Upscaling lattice Boltzmann and discrete element simulations for porous media

WaiChing Sun, PhD

Columbia University

The purpose of this lecture note is to provide a brief overview of the state-of-the-art multiscale techniques that utilize the lattice Boltzmann for flow simulations and the discrete element simulations for simulating the granular system fully saturated with pore fluid. We will review the basics of discrete element and lattice Boltzmann methods, the different options for multiscale coupling, and the recent research trend for more accurate and fast predictions for the multiscale modeling of porous media.

1 Introduction

From the bone remodeling to the failure of landslides, the micro-mechanical coupling between the solid skeleton and the pore fluid plays an important role to the macroscopic mechanical outcomes. While there are numerous works dedicated to model the interaction of the solid and fluid constituents at the representative element volume scale where continuum models are valid, the recent advancement of computational resource has made it possible to replicate the coupling mechanisms of the pore fluid and solid at the macroscopic scales. This lecture note provides a brief overview of the theoretical framework and numerical treatment that enables the linkage between the microscopic particle-fluid interactions and the macroscopic responses of the mixture continua.

Th rest of this lecture note is organized in 4 sections. We begin this lecture note with a brief review of the discrete element method for the granular materials and the lattice Boltzmann method for the pore fluid flow. We then present the multiscale techniques used to upscale the homogenized constitutive responses inferred from the representative elementary volume to the bulk and interface effective media. Each section ends with numerical examples used to verify the implementations and demonstrate the proper usages of the mathematical models.

As for notations and symbols, bold-faced letters denote tensors; the symbol '$\cdot$' denotes a single contraction of adjacent indices of two tensors (e.g. $\boldsymbol{a}\cdot\boldsymbol{b}=a_ib_i$ or $\boldsymbol{c}\cdot\boldsymbol{d}=c_{ij}d_{jk}$); the symbol ':' denotes a double contraction of adjacent indices of a tensor of rank two or higher (e.g. $\boldsymbol{C}:\boldsymbol{\epsilon}^e=C_{ijkl}\epsilon^e_{kl}$); the symbol '$\otimes$' denotes a juxtaposition of two vectors (e.g. $\boldsymbol{a}\otimes\boldsymbol{b}=a_ib_j$) or two symmetric second-order tensors (e.g. $(\boldsymbol{\alpha}\otimes\boldsymbol{\beta})_{ijkl}=\alpha_{ij}\beta_{kl}$). Moreover, $(\boldsymbol{\alpha}\oplus\boldsymbol{\beta})_{ijkl}=\alpha_{jl}\beta_{ik}$ and $(\boldsymbol{\alpha}\ominus\boldsymbol{\beta})_{ijkl}=\alpha_{il}\beta_{jk}$. We also define identity tensors $(\boldsymbol{I})_{ij}=\delta_{ij}$, $(\boldsymbol{I}^4)_{ijkl}=\delta_{ik}\delta_{jl}$, and $(\boldsymbol{I}^4_{\mathrm{sym}})_{ijkl}=\frac{1}{2}(\delta_{ik}\delta_{jl}+\delta_{il}\delta_{kj})$, where δ_{ij} is the Kronecker delta. As for sign conventions, unless specify otherwise, we consider the direction of the tensile stress and dilative pressure as positive.

2 Discrete element method for solid skeleton

To obtain effective stress measure from the DEM, we constitute a microscopic problem in which the macroscopic deformation measure is recast as the boundary condition for the unit problem. The unit cell problem is used to replace the macroscopic constitutive model that relates macroscopic strain measure and internal variables with the macroscopic effective stress measure. In the DEM model we employed, there is no microscopic internal variable introduced for the contact laws. Instead, path dependent behavior is mainly caused by the rearrangement of the grain contacts and the evolution of the force chain network topology.

In the unit cell DEM problem, the frame or walls of the particle assemblies are driven to move according to the macroscopic deformation measure via applying boundary traction or prescribing displacements on boundary particles [MDZ10, GZ14]. The contact forces are computed for each particle and the equations of motion are integrated by an explicit time integrator [CS79]. In quasi-static problems, to achieve static equilibrium of the particle assemblies, a dynamic relaxation scheme is employed.

Consider two rigid spheres p and q with radii R_p and R_q modeling a particle pair in contact inside a granular assembly. Let $\boldsymbol{y}_p$ and $\boldsymbol{y}_q$ denote the position vectors of their centers in a global coordinate system, while their orientations are represented by unit orientation quaternions $\boldsymbol{q}_p$ and $\boldsymbol{q}_q$ [ŠCC+10]. The relative velocity $\dot{\boldsymbol{d}}_t$ of the contact point $\boldsymbol{y}_c$ depends on the rate of change of the position vectors $\dot{\boldsymbol{y}}_p$ and $\dot{\boldsymbol{y}}_q$ and the rate of change of the particle orientations $\boldsymbol{w}_p$ and $\boldsymbol{w}_q$, i.e.,

$$\dot{\boldsymbol{d}}_t=\dot{\boldsymbol{y}}_q-\dot{\boldsymbol{y}}_p-\boldsymbol{w}_q\times(\boldsymbol{y}_c-\boldsymbol{y}_q)-\boldsymbol{w}_p\times(\boldsymbol{y}_c-\boldsymbol{y}_p) \tag{1}$$

Assuming that the contact areas of all particle pairs are infinitesimal and neglecting the gravitational force, and we also don't consider torques/couples at contacts due to rolling and torsion in the numerical examples in this paper, the

equations of motion for the translational and rotational degrees of freedom of particle p reads,

$$\begin{cases} m_p \ddot{\boldsymbol{y}}_p = \boldsymbol{f}_p = \sum_c^{n_c} \boldsymbol{f}_p^c \\ I_p \dot{\boldsymbol{w}}_p = \boldsymbol{t}_p = \sum_c^{n_c} (\boldsymbol{y}_c - \boldsymbol{y}_p) \times \boldsymbol{f}_p^c \end{cases} \tag{2}$$

with the mass m_p and moment of inertia I_p of the sphere p, $\boldsymbol{f}_p$ the sum of n_c contact forces $\boldsymbol{f}_p^c$ and $\boldsymbol{t}_p$ the sum of n_c contact torques due to tangential forces.

In YADE, following the form of Cundall's global damping [CS79], artificial numerical damping forces and torques are applied on each particle to reduce the total force and total torque that increases kinematic energy, while introducing damping to all eigen-frequencies [ŠCC+10]. The damping force $\boldsymbol{f}_p^{\text{damp}}$ on particle p is a function of the total contact force $\boldsymbol{f}_p$, the particle velocity $\dot{\boldsymbol{y}}_p$ and a dimensionless damping coefficient λ_{damp} (which we set to be 0.2 for all numerical examples presented in this paper). The damping torque $\boldsymbol{t}_p^{\text{damp}}$ on the rotational degree of freedom is constructed in a similar way, i.e.,

$$\begin{cases} \boldsymbol{f}_p^{\text{damp}} = -\lambda_{\text{damp}} \, \boldsymbol{f}_p \, \operatorname{sgn}(\boldsymbol{f}_p \cdot \dot{\boldsymbol{y}}_p) \\ \boldsymbol{t}_p^{\text{damp}} = -\lambda_{\text{damp}} \, \boldsymbol{t}_p \, \operatorname{sgn}(\boldsymbol{t}_p \cdot \dot{\boldsymbol{w}}_p) \end{cases} \tag{3}$$

.

Finally, (2) is integrated with a central difference scheme. Consider the incremental update from time step t to time step $t + \Delta t$ and let $(\boldsymbol{y}_p)_{t-\Delta t}$, $(\boldsymbol{y}_p)_t$, $(\boldsymbol{y}_p)_{t+\Delta t}$ denote the translational degrees of freedom for the p-th particle in three consecutive time steps. The explicit central difference scheme that updates $(\boldsymbol{y}_p)_{t+\Delta t}$ reads,

$$(\boldsymbol{y}_p)_{t+\Delta t} = \frac{1}{m_p} \left(\boldsymbol{f}_p + \boldsymbol{f}_p^{\text{damp}}\right)_t \Delta t^2 + 2(\boldsymbol{y}_p)_t - (\boldsymbol{y}_p)_{t-\Delta t} \tag{4}$$

For updating the orientation of the p-th particle $(\boldsymbol{q}_p)_{t+\Delta t}$, the explicit central difference scheme leads to the angular velocity at time $t + \frac{\Delta t}{2}$ [ŠCC+10],

$$(\boldsymbol{w}_p)_{t+\frac{\Delta t}{2}} = (\boldsymbol{w}_p)_{t-\frac{\Delta t}{2}} + \Delta t (\dot{\boldsymbol{w}}_p)_t = (\boldsymbol{w}_p)_{t-\frac{\Delta t}{2}} + \Delta t \frac{1}{I_p} \left(\boldsymbol{t}_p + \boldsymbol{t}_p^{\text{damp}}\right)_t \tag{5}$$

The Euler axis and angle of the rotation quaternion $\Delta \boldsymbol{q}_p$ are represented by a unit vector and the magnitude of the rotation $\Delta t (\boldsymbol{w}_p)_{t+\frac{\Delta t}{2}}$, respectively, i.e.,

$$\begin{cases} (\Delta \boldsymbol{q}_p)_{\boldsymbol{u}} = \widehat{(\boldsymbol{w}_p)_{t+\frac{\Delta t}{2}}} \\ (\Delta \boldsymbol{q}_p)_\theta = |\Delta t (\boldsymbol{w}_p)_{t+\frac{\Delta t}{2}}| \end{cases} \tag{6}$$

The rotation quaternion $(\boldsymbol{q}_p)_{t+\Delta t}$ is then updated by combining two rotation quaternions together, i.e.,

$$(\boldsymbol{q}_p)_{t+\Delta t} = \Delta \boldsymbol{q}_p (\boldsymbol{q}_p)_t \tag{7}$$

Note that the multiplication of quaternions is not commutative. Following the update of particle positions and orientations, the contact forces, moment are updated and the energy balance is checked. The static equilibrium is achieved when the particle velocity becomes sufficiently small. In YADE, this is indicated by the magnitude of the kinetic energy and the unbalanced force index (cf. [Ng06]).

In the actual numerical simulations, we employ a simple contact law model that can be decomposed into the normal and tangential components, $(\boldsymbol{f}_p^c)^n$ and $(\boldsymbol{f}_p^c)^t$ i.e.,

$$\sum_c^{n_c} \boldsymbol{f}_p^c = \sum_c^{n_c} \left((\boldsymbol{f}_p^c)^n + (\boldsymbol{f}_p^c)^t \right) \tag{8}$$

The normal contact force between a particle pair p and q is nonzero if and only if the particles are in contact, i.e.,

$$(\boldsymbol{f}_p^c)^n = (f_p^c)^n \boldsymbol{n} = \begin{cases} -k_n d_n \boldsymbol{n} \text{ if } d_n \leq 0 \\ 0 \text{ if } d_n > 0 \end{cases} ; \; d_n = \sqrt{(\boldsymbol{y}_p - \boldsymbol{y}_q) \cdot (\boldsymbol{y}_p - \boldsymbol{y}_q)} - R_p - R_q \tag{9}$$

where $\boldsymbol{n}$ is the contact normal vector, d_n is the overlapped length. Furthermore, the normal stiffness k_n of the grain contact is related to the radii (R_p and R_q) and Young's modulus of the particle E^g, i.e.,

$$k_n = 2 \frac{E^g R_p R_q}{R_p + R_q} \tag{10}$$

Meanwhile, the tangential force $(\boldsymbol{f}_p^c)^t$ depends on the shear stiffness k_t and the relative tangential displacement, but is also capped by the Coulomb's frictional force. As shown in [CCB14], the rate form of the tangential constitutive law reads,

$$\overset{\cdot}{(\boldsymbol{f}_p^c)^t} = \begin{cases} -k_t \dot{\boldsymbol{d}}_t \text{ if } ||k_t \dot{\boldsymbol{d}}_t|| \leq |(f_p^c)^n| \tan(\beta) \\ 0 \text{ if } ||k_t \dot{\boldsymbol{d}}_t|| > |(f_p^c)^n| \tan(\beta) \end{cases} ; \; k_t = A k_n \tag{11}$$

where c is the cohesion, A is a dimensionless material parameter, β is the friction angle.

Notice that the proposed multiscale coupling model is not limited to the DEM model with this particular set of constitutive laws.

RVE generation

The granular assemblies used in this study is obtained using the RVE generation engine available in an open source DEM software YADE [KD09]. In particular, we use the isotropic-compression method first introduced in [CS79]. For completeness, we briefly outline the procedure below:

1. First, a cell box with its six faces serving as the periodic boundaries is prepared. Spheres with defined particle size distribution are then randomly inserted into the box. Initially, these inserted particles are not allowed to overlap.
2. Material parameters of particles such as the contact stiffness, density and friction angle are then assigned to the particle. At this point, the assigned inter-particle friction coefficient is set to an artificial value to manipulate the amount of particle sliding and achieve the desired porosity. A large value of friction angle will yield a loosely packed RVE, and the value is set to a very low value when a dense packing is desired.
3. The unit cell is latter subjected to isotropic compression with prescribed confining pressure. The loading is carried out by an implemented engine which is capable of controlling either the Cauchy stress or the velocity gradient of the RVE. This process terminates when the entire RVE achieves static equilibrium.
4. Finally, the real values of friction coefficient are re-assigned to all particles and the RVE is now ready for future simulations.

If frictionless rigid walls are used as the RVE driving boundary, they are simply generated in the first step to replace the periodic box. As pointed out by [JKL03], the isotropic compression method is very efficient in generating dense granular assemblies. However, it is hard to maintain uniformity for loose specimens.

2.1 Numerical Example: successive sample reduction test for boundary condition sensitivity

The size of the unit cell (and therefore number of particles in the RVE) determines whether the apparent responses homogenized from microstructures of RVE could give converged coarse-scale effective properties. The size of the unit cell must be sufficiently large such that the apparent responses are insensitive to the imposed boundary condition [WLW08] and that it contains statistically enough mechanisms for the deformation processes. To ensure that the size of the unit cell is sufficiently large to be an RVE, we conduct a series of numerical experiments to empirically determine the representative element size. Following the ideas of successive sample tests discussed in [ZW01, WBF06, SAR11], we first create a large assembly composed of 979

equal-size spherical particles and obtain the local equilibrium state under a 100 kPa isotropic compression. Then we successively reduce the size of the cubic sampling window and obtain four other granular assembles with 619, 413, 311 and 75 particles. Four of these assemblies are shown in in Fig. 1. Each RVE is then brought to equilibrium state under confining pressure of 100 kPa. To analyze whether the granular assembly is homogeneous, we also plot the Rose diagram of the contact normal orientation and show them in Fig. 1. We observed that the the contact normals are distributed quite evenly in all assemblies, except the smallest one with 75 particles. This result is consistent with the finding on 2D granular assemblies reported in [GZ14] in which a granular assembly consisting of too few particles tends to exhibit more anisotropic responses. Nevertheless, the contact normal distribution also indicates that a few hundreds of particles may be enough to generate a dense assembly with a statistically homogeneous fabric.

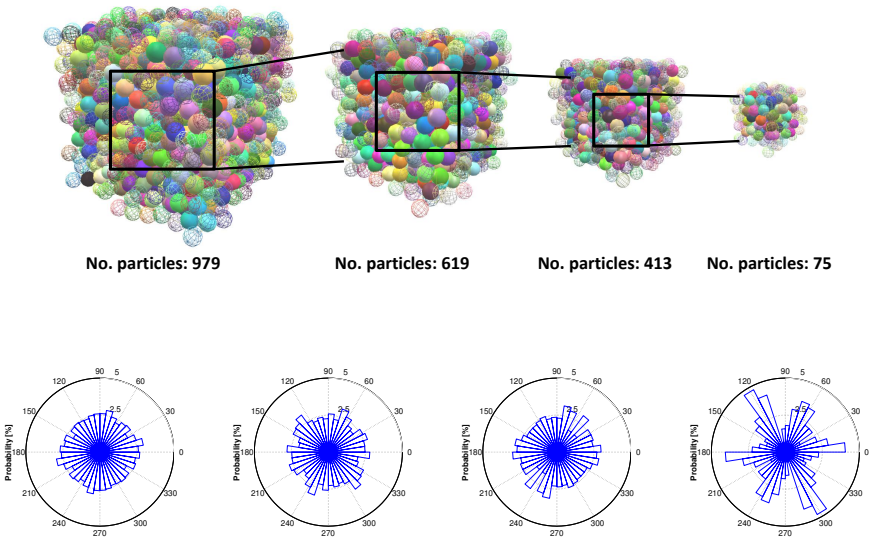

Figure 1: Four different sizes of granular assemblies used in the RVE study (UPPER) and the corresponding Rose diagram for contact normal orientation (LOWER).

All five numerical specimens are then subjected to triaxial loading until 20% axial strain. Previous studies have established that the boundary conditions driving the frame or surrounding wall of the unit cell may affect the macroscopic behavior. This sensitivity to the boundary condition is more severe

when the unit cell is smaller than the RVE size, but less important when the unit cell contains enough particles [ZW01, MD04, WBF06, WLW08, MDZ10, GZ14]. In particular, [MDZ10] has conducted systematic study to compare various constraints which transform periodic, linear displacement (zero rotation) and uniform stress to particle assemblies and found that all three satisfy a priori the Hill-Mandel condition. The study in [MDZ10] demonstrates that the linear displacement constraint produces the stiffest homogenized responses, the uniform stress constraint leads to the softest homogenized responses, while the periodic constraint leads to the intermediate response which is considered the optimal choice in [MD04]. In this study, we conduct numerical experiments for two types of boundary conditions, i.e. periodic boundary and frictionless rigid walls that impose linear displacement and zero rotation. The shear stress responses and porosity paths of triaxial compression tests on different size of RVEs are shown in Fig. 2.

3 Lattice Boltzmann method for fluid flow

A multi-scale lattice Boltzmann/Finite element method is used to extract geometrical features and permeability from the granular assemblies. This hybrid method was originally proposed in [WBF06] to estimate permeability of Castlegate Sandstone. Sun et al 2011a [SAR11] improved the accuracy and computation efficiency of this method by incorporating geometrical analysis in permeability calculations. The key to this improvement is partitioning the entire grain assembly into unit cells where pore-scale lattice Boltzmann simulations are conducted in the **connected** pores of each unit cell. Since discretized voxel images may contain isolated pore if the resolution is insufficient, this method is used to ensure that discretization does not alter connectivity of the pores.

The lattice Boltzmann method we used is a single-relaxation time BGK model [ZH97], which solves a discretized Boltzmann equation by simulating the evolution of particle distribution that propagates and collides locally among lattice nodes. The evolution of particle distribution function f_i in direction $\boldsymbol{e}_i$ is updated in each time step through the following equation,

$$f_i(\boldsymbol{x}+\boldsymbol{e}_i, t+\Delta t) - f_i(\boldsymbol{x}, t) = -\frac{1}{\tau}(f_i(\boldsymbol{x}, t) - f_i^{eq}(\boldsymbol{x}, t)) \tag{12}$$

where f^{eq} is a truncated equilibrium distribution defined as,

$$f_i^{eq} = w_i\rho(1 + \frac{3\boldsymbol{e}_i\cdot\boldsymbol{v}}{c_s^2} + \frac{9(\boldsymbol{e}_i\cdot\boldsymbol{v})^2}{c_s^4} - \frac{\boldsymbol{v}\cdot\boldsymbol{v}}{2c_s^2}) \tag{13}$$

τ is a parameter related to the dynamic fluid viscosity ν, as shown in the Chapman-Enskog equation (cf. [Suc01]),

$$\nu = \Delta t c_s^2(\tau - \frac{1}{2}) \tag{14}$$

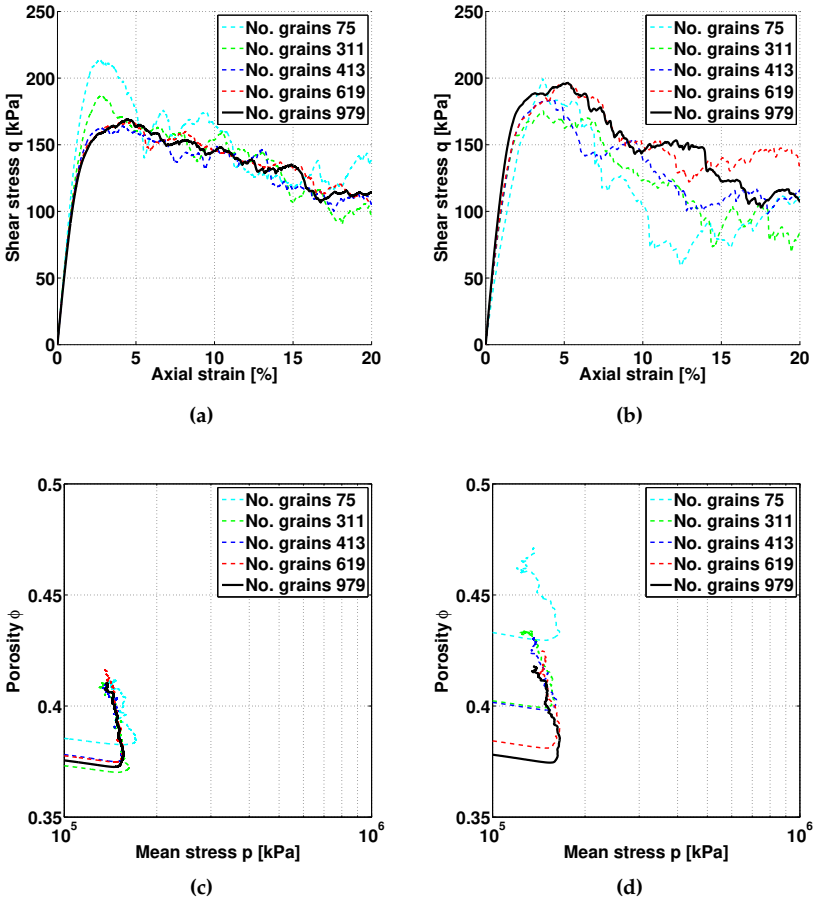

Figure 2: Shear stress response and porosity path of triaxial compression tests on different size of RVEs. (a)(c) RVE driven by periodic boundaries; (b)(d) RVE driven by frictionless rigid walls

where c_s is the constant speed of sound. *rho* and v are the macroscopic density and velocity. They are determined from the evolution of the particle distribution, i.e.,

$$\rho = \sum_{i=1}^{N} f_i \ ; \ v = \frac{1}{\rho} \sum_{i}^{N} f_i e_i \tag{15}$$

The effective permeability of a porous medium can be measured by applying a pore pressure gradient along a basis direction and determining the resultant fluid filtration velocity from a pore-scale hydrodynamics simulation. Then,

the effective permeability tensor is obtained according to,

$$k_{ij} = -\frac{\mu^v}{(\nabla^x p)_j} \frac{1}{V_\Omega} \int_\Omega v_i(\boldsymbol{x}) d\Omega \tag{16}$$

where μ^v is the kinematic viscosity of the fluid occupying the spatial domain of the porous medium Ω. To implement this procedure, we first assume that the effective permeability tensor k_{ij} is symmetric and positive definite. We then determine the diagonal components of the effective permeability tensor k_{ii} by three hydrodynamics simulations. In each simulation, we impose a pressure gradient on two opposite faces orthogonal to an axis $\boldsymbol{e}_i$ and no-slip boundary conditions on the four sides parallel to $\boldsymbol{e}_i$ where $\boldsymbol{e}_i$ denotes an orthogonal axis of a Cartesian system.

3.1 Numerical example 1: occluded porosity and its impact on homogenized permeability

In many situations, particularly in natural porous materials, occluded porosity occupies a significant portion of the pore space. Failure to identify occluded porosity can cause dramatic errors in multiscale modes. Typical situations where significant occluded porosity is expected to play a role include the migration of pore-fill cement into pore space, pore closure in limestones due to CO_2 sequestration, and the formation of compaction bands [SARE11].

To illustrate this point, let us consider a two dimensional LB simulation of the sample depicted in Figure 3. In this example, our objective is to obtain the vertical global permeability of a sample, discretized using a 30 u $\times$ 40 u lattice (u =lattice unit), using three different techniques. In the first technique, LB simulations are conducted on the entire sample, without any domain decomposition. This is equivalent to a direct numerical simulation and is interpreted here as the 'true' solution. The second technique uses domain decomposition (sample is split into four parts along the vertical direction) and uses occluded space detection, keeping only connected porosity active. The third technique uses domain decomposition but does not distinguish between connected and occluded porosity. Global permeabilities for the partitioned samples are obtained from the local estimates by [BBM87],

$$k = \frac{\sum_{i=1}^{n} L_i}{\sum_{i=1}^{n} L_i / k_i} \tag{17}$$

where k_i are the local values of permeability in each layer of thickness L_i, and $n = 4$ denotes the number of unit cells (layers).

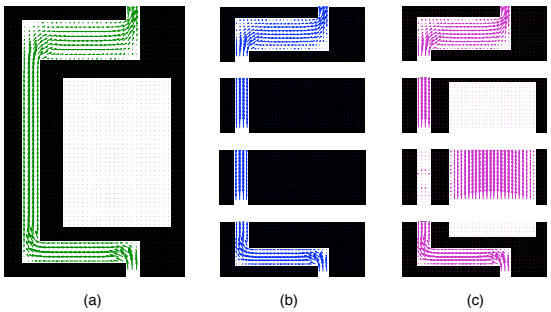

Figure 3: Velocity profiles of lattice Boltzmann simulations on (a) unpartitioned domain ($k = 0.015\ u^2$), (b) partitioned domain with identified and deactivated occluded porosity ($k = 0.013\ u^2$), and (c) partitioned domain without any special treatment for occluded porosity ($k = 0.0078\ u^2$). Where u =lattice unit.

Results for the LB calculations are summarized in Table 1. It should be highlighted that the relative error induced by the third procedure with partition but no special treatment of occluded porosity yielded an error four times greater than that of the partitioned method that takes into account occluded porosity. It can be seen from Table 1 that the main sources of error come from the mistreatment of occluded porosities in the central partitions. The mistreatment of occluded porosity is not only the source of errors in the estimation of permeability, but it leads to longer calculations as occluded porosity is assigned active lattices. Hence, not accounting for occluded porosity may lead to inaccuracies and inefficiencies.

Case	1	2	3
Number of Unit Cell(s)	1	4	4
Occluded Pore Identified?	No	Yes	No
Local Permeability, u^2 (top)	N/A	0.011	0.011
Local Permeability, u^2 (2nd top)	N/A	0.015	0.0029
Local Permeability, u^2 (2nd bottom)	N/A	0.015	0.45
Local Permeability, u^2 (bottom)	N/A	0.014	0.014
Global Permeability, u^2	0.015	0.013	0.0078
Relative Error	0	12 %	48 %

Table 1: Global and local permeabilities obtained from LB simulation scenarios.

3.2 Numerical Example 2: Verification against periodic simple cubic (SC) lattice

Simple cubic (SC) cells can be formed by placing the centroid of eight identical spheres at the corners of a cube of equal dimensions. When the spheres are making point contact, it is often called SC bead pack [SSD95]. In this packing, the total porosity is simply $\phi^f = 1 - \pi/6$ and the geometrical tortuosity is simply unity, as the shortest flow path is one directly though the center of the cell. Furthermore, as in other simple packings, all porosity is connected.

Unlike micro-structural attributes. permeability of SC packings cannot be directly obtained using analytical techniques. Instead, numerical procedures are often employed. The closest analytical solutions are furnished by bounds, such as the lower bound obtained by Dormieux and co-workers [DKU06] where pore spaces are ordered in the sense of inclusions and the permeability of a cylinder with cross-section made up by four circles examined. Since the cylindrical pore space is a subset of that of the SC cell, the permeability of the cylindrical pore space serves as a lower bound for that of the SC cell. The lower bound can be expressed in dimensionless form as $k \geq 4.84 \times 10^{-3} R^2$, where R is the radius of the spheres in the SC cell. Naturally, the permeability tensor in the SC cell is isotropic. Additionally, Zick and Homsy [ZH82] have analyzed the permeability of the SC bead pack by reducing the Navier-Stokes equation to a set of Fredholm integral equations. They found $k = 5.04 \times 10^{-3} R^2$.

Next, we calculate the effective permeability of the SC bead pack. Our first task is to correctly identify the connected porosity in the sample. The pore geometry is discretized in the usual way using a lattice mesh. The resolution of the lattice, clearly affects the results of the computations. The center of the pore space is selected as the first active lattice and porosity is determined using the region-growing algorithm. Figure 4 shows the estimate of porosity as a function of the lattice resolution. Once the voxel length is smaller that $R/50$, the numerical solution closely captures the exact solution $(1 - \pi/6)$.

Using a resolution of $R/50$, the resultant level set function and the shortest flow path are illustrated in Figure 5. As shown in the figure, in this simple example the geometrical tortuosity is unity and Dijkstra's algorithm is able to obtain this result without any issues. Finally, turning our attention to the effective permeability calculation, we obtain an estimate using lattice Boltzman at the aforementioned lattice resolution. In addition, we carried out a three dimensional Navier-Stokes finite element simulation to examine the reproducibility of the permeability calculation. The FE model is composed of 8937 tetrahedral Crouzeix-Raviat elements with non-periodic side walls ans prescribed pressures on the top and bottom faces of the cubic domain. The FE model was solved using an open-source differential solver called FEniCS [LMW12].

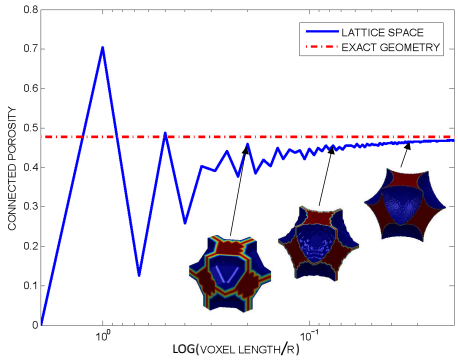

Figure 4: Connected porosity as a function of voxel length in a SC bead packing.

Figure 6 illustrates the results of the LB and FE simulations. The permeability using LB and FE is estimated to be $4.64 \times 10^{-3}R^2$ and $4.89 \times 10^{-3}R^2$, respectively. Since both methods are inherently different, and since the calculations are close to the previous values of permeability estimated for SC packings, we consider the 5.1% difference in solutions acceptable. We therefore conclude that the proposed framework to estimate permeability based on level sets and lattice Boltzmann is accurate.

4 Multiscale homogenization for bulk porous media

In this section, we describe the homogenization theory we adopt to establish the DEM-mixed-FEM coupling model for fully saturated porous media. Previous work for dry granular materials, such as [MD04, MDZ10, NCDD11, GZ14], has demonstrated that a hierarchical discrete-continuum coupling model can be established by using grain-scale simulations to provide Gauss point stress update for finite element simulations in a fully implicit scheme. Nevertheless, the extension of this idea for partially or fully saturated porous media has not been explored, to the best knowledge of the authors.

In this work, we hypothesize that the pore-fluid flow inside the pores is in the laminar regime and is dominated by viscous forces such that Darcy's law is valid at the representative elementary volume level [SARE11, SAR11, SKR13]. Provided that this assumption is valid, we define the pore pressure field only at the macroscopic level and neglect local fluctuation of the pore pressure at the pore- and grain-scale.

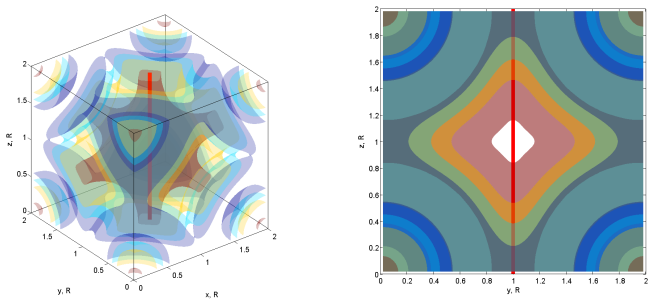

Figure 5: Level set function $\phi(x,y,z)$ (represented by the 3D color contour) and the corresponding shortest flow path (represented by the red straight line) as determined by Dijkstra's algorithm.

On the other hand, we abandon the usage of macroscopic constitutive law to replicate the constitutive responses of the solid constituent. Instead, we apply the effective stress principle [TTE+43, GSP09, GMS13] and thus allow the change of the macroscopic effective stress as a direct consequence of the compression, deformation and shear resistance of the solid constituent inferred from grain-scale simulations. As a result, the effective stress can be obtained from homogenizing the forces and branch vectors of the force network formed by the solid particles or aggregates, while the total stress becomes a partition of the homogenized effective stress from the microscopic granular assemblies, and the pore pressure from the macroscopic mixture continuum.

4.1 Dual-scale effective stress principle

In this study, we make assumptions that (1) a separation of scale exists and that (2) a representative volume element (RVE) can be clearly defined. Strictly speaking, the assumption (2) is true if the unit cell has a periodic microstructure or when the volume is sufficiently large such that it possesses statistically homogeneous and ergodic properties [GAS07].

With the aforementioned assumptions in mind, we consider a homogenized macroscopic solid skeleton continuum $\mathcal{B}^s \subset \mathbb{R}^3$ whose displacement field is C^0 continuous. Each position of the macroscopic solid body in the reference configuration, i.e., $\boldsymbol{X} = \boldsymbol{X}^s \in \mathcal{B}_0^s$, is associated with a micro-structure of the RVE size. Let us denote the trajectories of the macroscopic solid skeleton and the fluid constituent in the saturated two-phase porous medium from the reference configuration to the current solid configuration as,

$$\boldsymbol{x} = \boldsymbol{\varphi}^s(\boldsymbol{X},t) \;;\; \boldsymbol{x} = \boldsymbol{\varphi}^f(\boldsymbol{X}^f,t) \tag{18}$$

Unless the porous medium is locally undrained, the solid and fluid constituents are not bundled to move along the same trajectory, i.e., $\boldsymbol{\varphi}^s(\cdot,t) \neq$

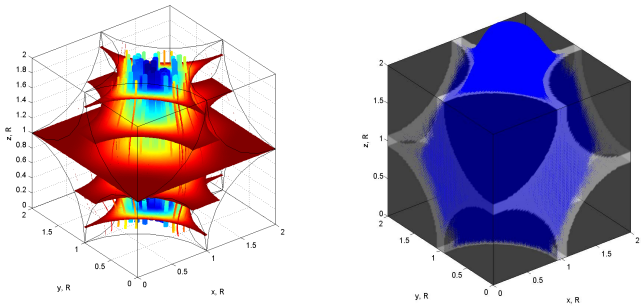

(a) (b)

Figure 6: (a) Streamline of the simple cubic lattice computed via Stokes finite element model ($k = 4.89 \times 10^{-3} R^2$). (b) Velocity profile of the simple cubic lattice obtained via lattice Boltzmann simulation conducted on connected pore space ($k = 4.64 \times 10^{-3} R^2$).

$\boldsymbol{\varphi}^f(\cdot, t)$. If we choose to follow the macroscopic solid skeleton trajectory to formulate the macroscopic balance principles, then the control volumes are attached to solid skeleton only, and the pore fluid motion is described by relative movement between the fluid constituent and the solid matrix, as shown in Fig. 7. The deformation gradient of the macroscopic solid constituent $\boldsymbol{F}$ can therefore be written as,

$$\boldsymbol{F} = \frac{\partial \boldsymbol{\varphi}(\boldsymbol{X}^s, t)}{\partial \boldsymbol{X}^s} = \frac{\partial \boldsymbol{\varphi}(\boldsymbol{X}, t)}{\partial \boldsymbol{X}} = \frac{\partial \boldsymbol{x}}{\partial \boldsymbol{X}} \tag{19}$$

in which we omit the superscript s when quantities are referred to solid phase. Now, following [MD04], we associate each point in the current configuration $\boldsymbol{x}$ with an aggregate of N particles inside the representative volume $\mathcal{V}$. Furthermore, we introduce a local coordinate system for the RVE in which the position vector $\boldsymbol{y} \in \mathbb{R}^3$ becomes $\boldsymbol{0}$ at the geometric centroid of the RVE. The locations of the centroids of the N particles expressed using the local coordinate system read, i.e.,

$$\boldsymbol{y}_p \in \mathcal{V}, \;\; p = 1, 2, ...N. \tag{20}$$

where $\boldsymbol{y}_p$ is the local position vector of the center of the p-th particle in the microstructure and $\boldsymbol{x} + \boldsymbol{y}_p$ is the same position expressed in the macroscopic current coordinate system. Particles inside the RVE may make contacts to each other. The local position vector of each contact between each particle-pair $\boldsymbol{y}_c$ can be written as,

$$\boldsymbol{y}_c \in \mathcal{V}, \;\; c = 1, 2, ...N_c. \tag{21}$$

Both the positions of the particles $\boldsymbol{y}_p$ and that of the contacts $\boldsymbol{y}_c$ are governed by contact law and the equilibrium equations. Previous works, such as

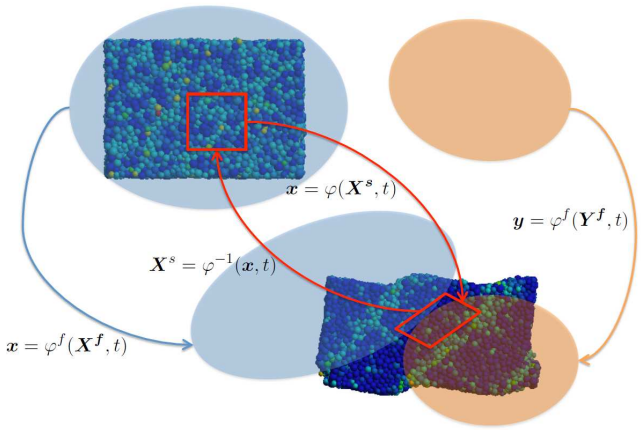

Figure 7: Trajectories of the solid and fluid constituents $\boldsymbol{\varphi}^s = \boldsymbol{\varphi}$ and $\boldsymbol{\varphi}^f$. The motion $\boldsymbol{\varphi}$ conserves all the mass of the solid constituent, while the fluid may enter or leave the body of the solid constituent. Figure reproduced from [SOS13]

.

[CVW04, ESZ05, HC11, GTSMW13, RRL14, CLCC14], have found success in explicitly modeling the pore-scale grain-fluid interaction. Nevertheless, such grain-fluid interaction simulations do impose a very high computational demand due to the fact that the fluid flow typically requires at least an order more of degree of freedoms to resolve the flow in the void space among particles. However, for seepage flow that is within the laminar regime where Darcy's law applies, the new insight obtained from the costly simulations will be limited. As a result, this discrete-continuum coupling model does not explicitly model the pore-scale solid-fluid interaction. Instead, we rely on the hypothesis that effective stress principle is valid for the specific boundary value problems we considered. In particular, we make the following assumptions:

- The void space is always fully saturated with one type of fluid and there is no capillary effect that leads to apparent cohesion of the solid skeleton.
- The flow in the void space remains Darcian at the macroscopic level.
- All particles in the granular assemblies are in contact with the neighboring particles.
- Fluidization, suffusion and erosion do not occur.
- Grain crushing does not occur.

- There is no mass exchange between the fluid and solid constituents.

As a result, we may express the total macroscopic Cauchy stress as a function of homogenized Cauchy effective stress inferred from DEM and the macroscopic pore pressure obtained from the mixed finite element, i.e.

$$\boldsymbol{\sigma}(\boldsymbol{x},t) =< \boldsymbol{\sigma}'(\boldsymbol{x},t) >_{\mathrm{RVE}} -B(\boldsymbol{x},t)p^f(\boldsymbol{x},\boldsymbol{t})\boldsymbol{I} \tag{22}$$

where

$$< \boldsymbol{\sigma}'(\boldsymbol{x},t) >_{\mathrm{RVE}} = \frac{1}{2\mathrm{V}_{\mathrm{RVE}}} \sum_{c}^{Nc} (\boldsymbol{f}^c \otimes \boldsymbol{l}^c + \boldsymbol{l}^c \otimes \boldsymbol{f}^c) \tag{23}$$

$\boldsymbol{f}^c$ is the contact force and $\boldsymbol{l}^c$ is the branch vector, the vector that connects the centroids of two grains forming the contact [CMNN81, Bag96, SKR13], at the grain contact $\boldsymbol{x} + \boldsymbol{y}_c \in \mathbb{R}^3$. V_{RVE} is the volume of the RVE and N_c is the total number of particles in the RVE. Meanwhile, the Biot's coefficient B reads,

$$B(\boldsymbol{x},\boldsymbol{t}) = 1 - \frac{K_T^{\mathrm{DEM}}(\boldsymbol{x},t)}{K_s} \tag{24}$$

with $K_T^{\mathrm{DEM}}(\boldsymbol{x},t)$ and K_s being the effective tangential bulk modulus of the solid matrix inferred from DEM, and the bulk modulus of the solid grain respectively [NB71, SWZP86]. Notice that, in the geotechnical engineering and geomechanics literature, such as [Ng06, KRMK14], it is common to impose incompressible volumetric constraint on dry DEM assembly to simulate undrained condition at meso-scale. This treatment can be considered as a special case of (24) when the bulk modulus of the solid grain is significantly higher than that of the skeleton such that the Biot's coefficient is approximately equal to one.

4.2 Micro-macro-transition for solid skeleton

In this study, we consider the class of two-phase porous media of which the solid skeleton is composed of particles. These particles can be cohesion-less or cohesive, but the assemblies they formed are assumed to be of particulate nature and hence suitable for DEM simulations. [CS79].

In our implementation, the DEM simulations are conducted via YADE (Yet Another Dynamic Engine [ŠCC+10]), an open source code base for discontinua. These grain-scale DEM simulations are used as a replacement to the macroscopic constitutive laws that relate strain measure with effective stress measure for each RVE associated with a Gauss point in the macroscopic mixed finite element. In particular, a velocity gradient is prescribed to move the frame of the unit cell and the DEM will seek for the static equilibrium state via dynamics relaxation method. After static equilibrium is achieved, the internal forces and branch vectors are used to compute the homogenized effective Cauchy stress via the micro-macro transition theory [MD04, MDZ10, WLW08].

For completeness, we provide a brief overview of DEM, the procedure for generation of RVEs and the study on the size of RVEs in Appendix A,B and C.

The Hill-Mandel micro-heterogeneity condition demands that the power at the microscopic scale must be equal to the the rate of work done measured by the macroscopic effective stress and strain rate measures. For the solid constituent of the two-phase porous media, this condition can be expressed in terms of any power-conjugate effective stress and strain rate pair , such as $(\boldsymbol{P}', \dot{\boldsymbol{F}})$ and $(\boldsymbol{S}', \dot{\boldsymbol{E}})$ and $(\boldsymbol{\sigma}', \boldsymbol{D})$ [BA95, Arm99]. For instance, the condition can be written in terms of the effective stress and rate of deformation of the solid skeleton, i.e.,

$$< \boldsymbol{\sigma}' >_{\mathrm{RVE}} : < \boldsymbol{D} >_{\mathrm{RVE}} = < \boldsymbol{\sigma}' : \boldsymbol{D} >_{\mathrm{RVE}} \tag{25}$$

where $\boldsymbol{D}$ is the rate of deformation, i.e., the symmetric part of the velocity gradient tensor,

$$< \boldsymbol{D} >_{\mathrm{RVE}} = \frac{1}{2}(< \boldsymbol{L} >_{\mathrm{RVE}} + < \boldsymbol{L}^{\mathrm{T}} >_{\mathrm{RVE}}) \; ; \; \boldsymbol{L} = \boldsymbol{\nabla}^{\boldsymbol{x}} \boldsymbol{v} \tag{26}$$

and $< \boldsymbol{\sigma}' >_{\mathrm{RVE}}$ is defined previously in (23). Previous studies, such as, [MD04, WLW08, MDZ10, Fis13], have established that the linear deformation, periodic, and uniform traction are three boundary conditions that satisfy the Hill-Mandel micro-heterogeneity condition. In our implementation, we apply the periodic boundary condition to obtain the effective stress measure, because the periodic boundary condition may yield responses that are softer than those obtained from the linear deformation BC but stiffer than those obtained from the uniform traction BC. In particular, the periodic boundary condition enforces two constraints: (1) the periodicity of the deformation, i.e.,

$$[[\boldsymbol{y}_b]] = < \boldsymbol{F} >_{\mathrm{RVE}} [[\boldsymbol{Y}_b]] \text{ and } [[\boldsymbol{R}_b]] = \boldsymbol{0} \tag{27}$$

where $[[\cdot]]$ denotes the jump across boundaries, $\boldsymbol{y}_b$ and $\boldsymbol{Y}_b$ represent the position vectors of the particles at the boundary of the reference and current configurations, $R_b \in SO(3)$ represents the rotation tensor of particles at the boundary, and (2) the anti-periodicity of the force $\boldsymbol{f}_b$ and moment on the boundary of the RVE, i.e.,

$$[[\boldsymbol{f}_b]] = \boldsymbol{0} \text{ and } [[(\boldsymbol{y}_c - \boldsymbol{y}_b) \times \boldsymbol{f}_b]] = \boldsymbol{0} \tag{28}$$

In YADE, the DEM code we employed for grain-scale simulations, the deformation of an RVE is driven by a periodic cell box in which the macroscopic velocity gradient of the unit cell $< \boldsymbol{L} >_{\mathrm{RVE}}$ can both be measured and prescribed.

4.3 Multiscale hydro-mechanical model

The differential equations governing the isothermal saturated porous media in large deformation are derived based on the mixture theory, in which

solid matrix and pore fluid are treated together as a multiphase continuum [Pre82, BA95, Arm99, Cou04, SOS13, MNBT13]. The solid and fluid constituents may simultaneously occupy fractions of the volume of the same material point. The physical quantities of the mixture, such as density and total stress, are spatially homogenized from its components. For example, the averaged density of the fluid saturated soil mixture is defined as:

$$\rho = \rho^s + \rho^f = (1-\phi)\rho_s + \phi\rho_f \tag{29}$$

where ρ^α is the partial mass density of the α constituent and ρ_α is the intrinsic mass density of the α constituent, with ϕ being the porosity.

4.3.1 Balance of linear momentum

For the balance of linear momentum law in finite strain, we adopt the total Lagrangian formulation and choose the total second Piola-Kirchhoff stress (PK2) $\boldsymbol{S}$ as the stress measure. The inertial effect is neglected. The equation takes the form:

$$\nabla^{\boldsymbol{X}}\cdot(\boldsymbol{F}\boldsymbol{S}) + J(\rho^s + \rho^f)\boldsymbol{g} = \boldsymbol{0} \tag{30}$$

where the Jacobian $J = \det(\boldsymbol{F})$. The principle of effective stress postulates that the total Cauchy stress $\boldsymbol{\sigma}$ can be decomposed into an effective stress due to the solid skeleton deformation and an isotropic pore pressure (p^f) stress. The effective stress principle in terms of PK2 writes:

$$\boldsymbol{S} = \boldsymbol{S'}^{\mathrm{DEM}} - J\boldsymbol{F}^{-1}B^{\mathrm{DEM}}p^f\boldsymbol{I}\boldsymbol{F}^{-T} \tag{31}$$

where

$$\boldsymbol{S'}^{\mathrm{DEM}} = J\boldsymbol{F}^{-1}\boldsymbol{\sigma'}^{\mathrm{DEM}}\boldsymbol{F}^{-T} = J\boldsymbol{F}^{-1}\Big(\frac{1}{\mathrm{V_{RVE}}}\sum_i^{Nc}\boldsymbol{f}\otimes\boldsymbol{l}\Big)\boldsymbol{F}^{-T} \tag{32}$$

Thus the balance of linear momentum becomes:

$$\nabla^{\boldsymbol{X}}\cdot(\boldsymbol{F}\boldsymbol{S'}^{\mathrm{DEM}} - JB^{\mathrm{DEM}}p^f\boldsymbol{F}^{-T}) + J(\rho^s+\rho^f)\boldsymbol{g} = \boldsymbol{0} \tag{33}$$

4.3.2 Balance of fluid mass

The simplified u-p formulation in finite strain requires another equation illustrating the balance of mass for pore fluid constituent:

$$\frac{D\rho^f}{Dt} = -\nabla^{\boldsymbol{X}}\cdot(J\boldsymbol{F}^{-1}[\phi^{\mathrm{DEM}}\rho_f(\boldsymbol{v}^f - \boldsymbol{v})]) \tag{34}$$

where $\frac{D[\bullet]}{Dt} = [\dot{\bullet}]$ is the material time derivative with respect to the velocity of solid skeleton $\boldsymbol{v}$.

We make isothermal and barotropic assumptions and suppose that $p^f << K_s$ and that $\frac{DB^{\mathrm{DEM}}}{Dt} \sim 0$. After simplifications [SOS13], the balance of mass becomes:

$$\frac{B^{\mathrm{DEM}}}{J}\frac{DJ}{Dt} + \frac{1}{M^{\mathrm{DEM}}}\frac{Dp^f}{Dt} + \nabla^{\boldsymbol{X}}\cdot(\frac{1}{\rho_f}(J\boldsymbol{F}^{-\mathbf{1}}[\phi^{\mathrm{DEM}}\rho_f(\boldsymbol{v^f}-\boldsymbol{v})])) = 0 \tag{35}$$

where

$$M^{\mathrm{DEM}} = \frac{K_s K_f}{K_f(B^{\mathrm{DEM}} - \phi^{\mathrm{DEM}}) + K_s\phi^{\mathrm{DEM}}} \tag{36}$$

is the Biot's modulus [NB71], with K_f being the bulk modulus of pore fluid.

In this paper, Darcy's constitutive law relating the relative flow and the pore pressure is employed, neglecting the inertial effect:

$$\boldsymbol{Q} = \boldsymbol{K}^{\mathrm{DEM}}\cdot(-\nabla^{\boldsymbol{X}}\, p^f + \rho_f \boldsymbol{F}^{\mathrm{T}}\cdot\boldsymbol{g}) \tag{37}$$

where the pull-back permeability tensor $\boldsymbol{K}^{\mathrm{DEM}}$ is defined as

$$\boldsymbol{K}^{\mathrm{DEM}} = J\boldsymbol{F}^{-1}\cdot\boldsymbol{k}^{\mathrm{DEM}}\cdot\boldsymbol{F}^{-\mathrm{T}} \tag{38}$$

Assume that the effective permeability tensor $\boldsymbol{k}^{\mathrm{DEM}}$ is isotropic, i.e.,

$$\boldsymbol{k}^{\mathrm{DEM}} = k^{\mathrm{DEM}}\boldsymbol{I} \tag{39}$$

where k^{DEM} is the scalar effective permeability in unit of $\frac{m^2}{Pa\cdot s}$. It is updated from porosity of DEM RVEs according to the Kozeny-Carmen equation.

4.4 Numerical Example 1: Globally undrained shear test of dense and loose assemblies

For the second example we employ our multiscale scheme to perform shear tests on both dense and loose granular assemblies. The macroscopic geometry and boundary conditions are illustrated on a sample discretized by coarse mesh (1×5×5 in X,Y,Z directions) as Fig. 8. We also use a medium fine mesh (1×8×8) and a fine mesh (1×10×10) to investigate the mesh dependency issue of the proposed scheme. All results in this section are computed from the fine mesh model, if not specified. The nodes on the bottom boundary are fixed in all directions and those on the upper boundary are translated identically towards the positive y axis at a constant rate. They are maintained at a constant vertical stress $\sigma_z = 100kPa$ by a horizontal rigid layer (not shown). This constraint is imposed in the model by the Lagrange multiplier method. The lateral surfaces are constrained by frictionless rigid walls (not shown). All surfaces are impervious. The gravitational effect is not considered in this study. For coupled microscopic DEM models, periodic unit cells composed of uniform spheres are prepared by an isotropic compression engine in YADE

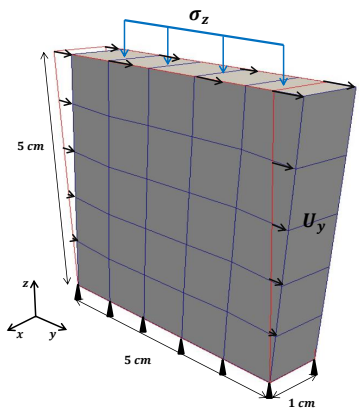

Figure 8: Geometry and boundary conditions for globally undrained shear test

up to $\sigma_{iso} = 100kPa$ with initial porosity of 0.375 and 0.427 for dense and loose assemblies respectively, and then are assigned identically to all the integration points of the FEM model before shearing.

The finite strain formulation is first adopted to study the hydro-mechanical coupling effect during the shearing of the dense and loose samples with undrained boundaries. The material parameters used in the simulations allowing hydraulic diffusion within the specimen are presented in Table 2. They are categorized into micromechanical material parameters used in DEM solver, poro and poro-plasticity parameters derived from DEM RVEs and macroscopic properties set in FEM. Note that the permeability k is updated with porosity of RVEs using the Kozeny-Carman relation during the simulation. To prevent local seepage of water within the samples, the permeability k is set to 0 $m^2/(Pa \cdot s)$.

Fig. 9 represents the global shear stress and volumetric strain behavior of shear simulations with and without local seepage of water. The strain-hardening behavior of undrained dense granular assemblies (left column) and strain-softening behavior of undrained loose granular assemblies (right column) are recovered [YIV98]. In both assemblies, when local seepage is prohibited, the shear stress immediately rises when the shearing begins and the saturated porous media behaves stiffer than the samples with local seepage. Note that the sudden drop in Fig. 9(b) is due to the unstable solid matrix of loosely confined DEM unit cell. The volumetric strain of the dense sample with seepage monotonically increases. This phenomenon is attributed to the

	Parameter	Value
Microscopic property in DEM	Solid grain normal stiffness k_n	$2.2 \times 10^6\ N/m$
	Solid grain tangential stiffness k_s	$1.9 \times 10^6\ N/m$
	Solid grain friction angle β	30°
	Solid grain bulk modulus K_s	0.33 GPa
Macroscopic property inferred from DEM	Porosity ϕ	dense: 0.375, loose: 0.427
	Biot's coefficient B	dense: 0.976, loose: 0.983
	Biot's Modulus M	dense: 180 Mpa, loose: 168 Mpa
Macroscopic property in FEM	Fluid bulk modulus K_f	0.1 GPa
	Initial permeability k	$1 \times 10^{-9}\ m^2/(Pa \cdot s)$
	Solid density ρ_s	$2700\ kg/m^3$
	Fluid density ρ_f	$1000\ kg/m^3$

Table 2: Material parameters in globally undrained shear problem

rearrangement of solid matrix as the grains tend to rise over adjacent grains when they are driven by shear forces. In absence of local diffusion, the dense sample experiences a reduction of volume instead, suggesting that the compression of overall solid matrix predominates the above phenomenon. As for loose samples, however, the volumetric behavior is opposite. When local diffusion of water is prohibited, the pore collapse and densification of local regions within specimen could occur, resulting in a compression at early stage of shearing before the dilatancy phenomenon. The curve of no-local-seepage case shows that the dilatancy phenomenon prevails all along the shearing. In all cases, the volume changes are beneath 0.12%, confirming that the samples are indeed sheared under globally undrained condition.

We examine the mesh dependency by three aforementioned mesh densities adopted in simulations of dense assembly with local seepage. The effect is presented via plots of global $\sigma_{yz} - \gamma_{yz}$ and $\varepsilon_v - \gamma_{yz}$ responses as Fig. 10. For stress response, discrepancy between medium and fine meshes is not significant, but coarse mesh apparently yields stiffer solution after 2% shear strain and the maximum deviation is about 7.6% with respect to the fine mesh solution. The differences between ε_v curves are less significant and do not exceed 4% of the fine mesh solution. Thus, our choice of the fine mesh to conduct numerical experiments is acceptable.

We next display the difference between the finite-strain and small-strain multiscale schemes in simulations of dense granular sample in both local diffusion conditions in Fig. 11. According to the global shear responses, the small strain and finite strain yield consistent solutions within 2% shear strain. Then the discrepancy gradually emerges and the introduction of geometrical nonlinearity renders the sample stiffer. This observation is the same as the conclusion in the previous Terzaghi's problem section. Finite strain solutions exhibit less volume changes in both cases. Moreover, geometrical non-linear term

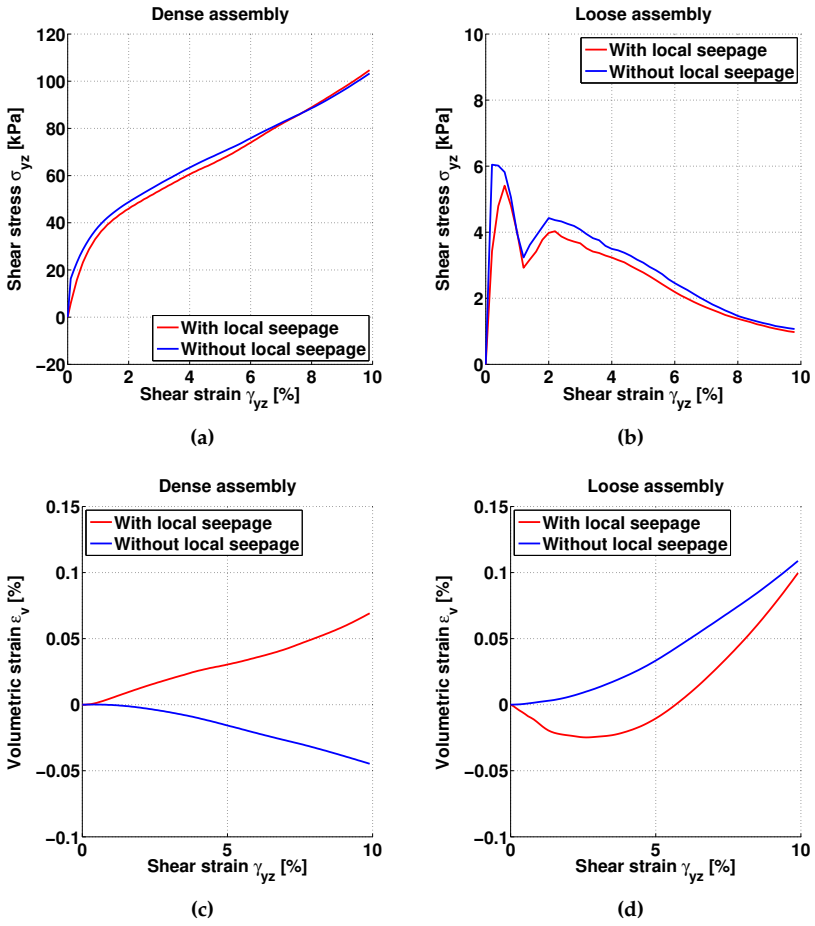

Figure 9: Comparison of global shear stress and volumetric strain behavior between globally undrained dense and loose assemblies with and without local diffusion

even alters the dilatancy behavior: the sample is computed to be compressed when no local seepage of water is allowed, while the small strain solution conserves the dilatant trend.

We also assess the local diffusion effect via color maps of pore pressure developed during the deformation, as shown in Fig. 12. The dense sample with local seepage has developed negative pore pressure and the pressure distribution is nearly uniform, since fluid flow could take place inside the specimen to dissipate pressure difference between neighboring pores. Without

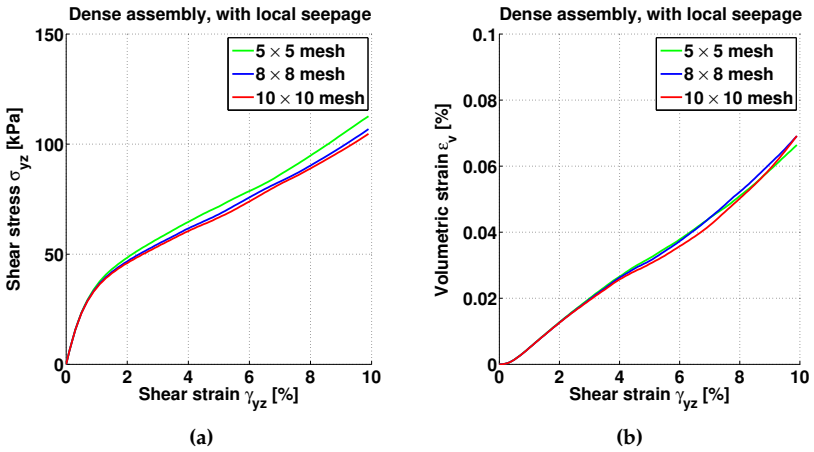

Figure 10: Comparison of global shear stress and global volumetric strain behavior between coarse mesh (1×5×5), medium mesh (1×8×8), fine mesh (1×10×10), finite strain formulation

local seepage of water, the pore pressure is concentrated to four corners of the sample, with the upper left and bottom right corners compressed (positive pressure) and the other two dilated (negative pressure). Furthermore, these corners have maximum pressure gradient $||\nabla p^f||$.

The multiscale nature of our method offers more insight into the local states of granular sample. With the granular material behavior homogenized from responses of RVEs, the grain displacements, the effective stress paths (shear stress $q = \sigma_1 - \sigma_3$ vs. effective mean stress $p' = \frac{\sigma_1+\sigma_2+\sigma_3}{3}$) and the volumetric strain paths (ε_v vs. p') in each DEM unit cell are directly accessible. As an example, the local distribution of q at the end of shearing for globally undrained yet locally diffused dense sample (13) shows a concentration of shear stress in upper left and bottom right corners, while the corners correspondent to the other diagonal sustain comparably very little shear stress. The deformed configuration of spheres in three representative RVEs are colored according to the dimensionless displacement magnitude $\frac{||\boldsymbol{u}||_2}{\text{inital size of unit cell}}$ compared to initial RVE configuration. We present stress paths of these three RVEs providing evidence that strain-softening (Fig. 14(a)), limited strain-softening (Fig. 14(b)) and strain-hardening (Fig. 14(c)) could locally occur in a dense sample which globally behaves in a strain-hardening manner. A critical state line $q = \eta p'$ is drawn for three stress paths and the value of slope η is identified as 1.16. η and the Mohr-Coulomb friction angle β' is computed to be 29.1° by the following

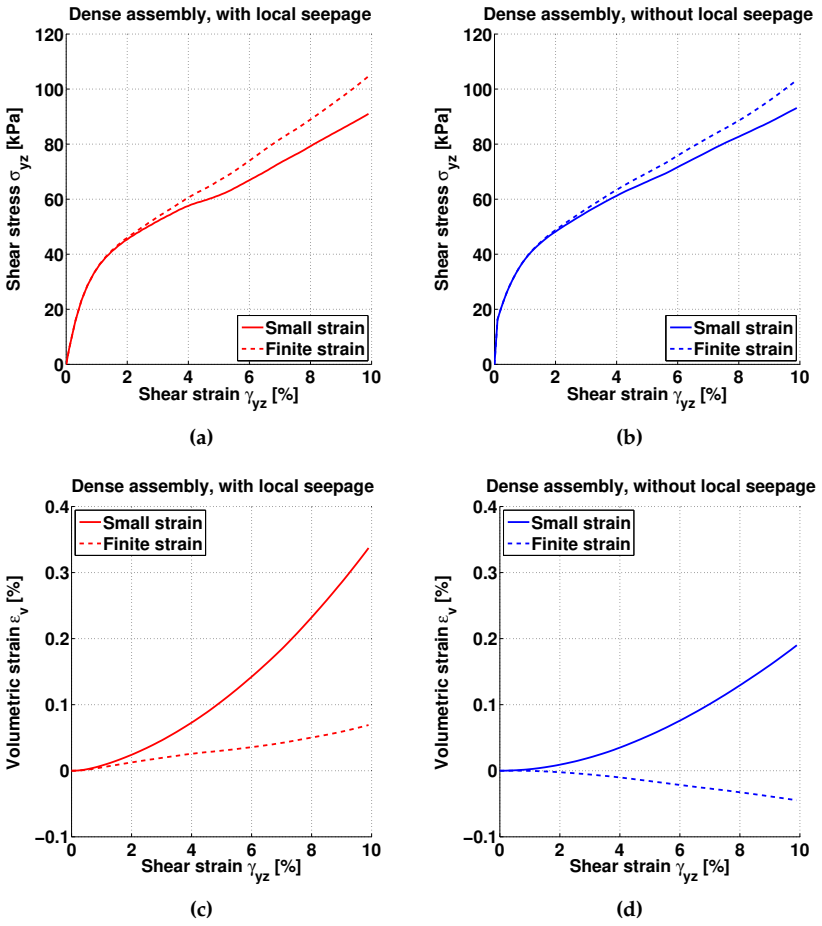

Figure 11: Comparison of global shear stress and global volumetric strain behavior between small strain and finite strain formulation. Left: globally undrained with local diffusion condition, Right: globally undrained but without local diffusion condition

relation for cohesionless soil [Woo90]:

$$\sin \beta' = \frac{3\eta}{6+\eta} \tag{40}$$

, which is close to the inter-particle friction angle $\beta = 30^\circ$. Paths of ε_v further demonstrate that large local volume change up to 5.5% is possible even globally the sample is only dilated about 0.07%. According to these figures, the small strain and finite strain shear responses are almost identical. The stress

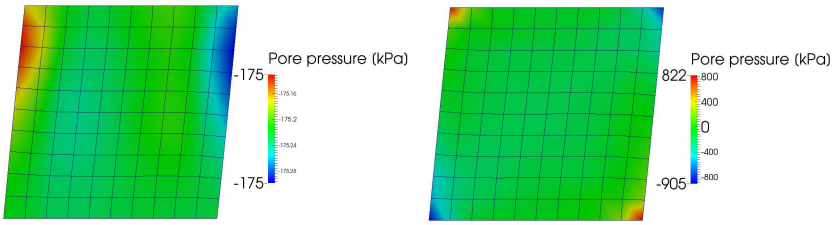

Figure 12: Comparison of pore pressure at 10% shear strain between (a) dense sample with local seepage and (b) dense sample without local seepage

path curves exhibit little difference. However, geometrical non-linearity has more significant effect on volumetric strain path. A major remark is that, inside the strain-softening spot as 14(d), the small strain solution has large fluctuation when the mean effective stress is very small, because DEM assemblies are highly unstable with nearly zero confining stress. On the contrary, finite strain scheme avoids this unstable regime and yield smooth solutions.

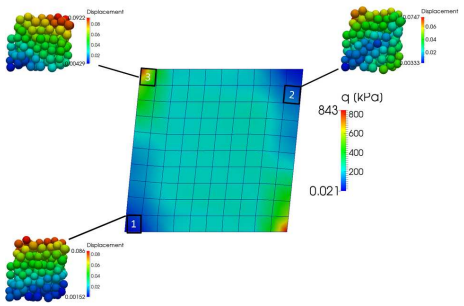

Figure 13: Spatial distribution of shear stress q at 10% shear strain for globally undrained dense sample allowing seepage within the specimen, attached with displacement magnitude of grains in unit cells (normalized by the initial cell size)

Lastly, we investigate the rate-dependent shearing behavior using the proposed coupling scheme. A faster shearing of saturated granular sample influences its mechanical response mainly by speeding up the solid matrix rearrangement and also by allowing less fluid diffusion inside the sample between loading steps. The former effect leads to swelling of the sample, while

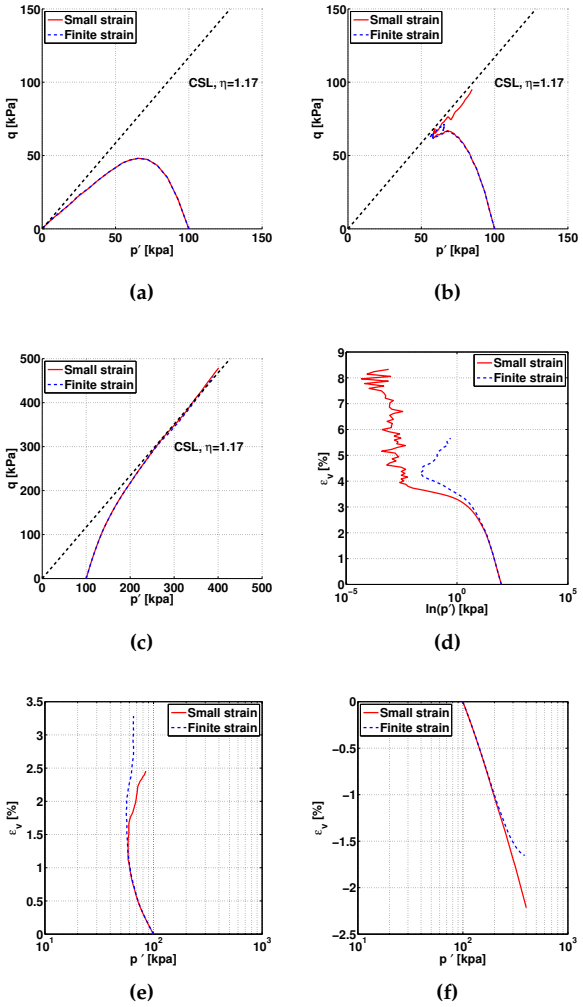

Figure 14: Shear stress vs. effective mean stress at different locations indexed as Fig. 13: (b) stress path at point 1 (c) stress path at point 2 (d) stress path at point 3; Volumetric strain vs. effective mean stress at different locations: (e) volume path at point 1 (f) volume path at point 2 (g) volume path at point 3

the latter renders the specimen more locally undrained. Fig.15 illustrates the combined effect of these two mechanisms on a dense sample with local seepage. The evolution of shear stress and volumetric strain with shearing rates of 0.1% and 0.5% per second are compared. When shearing is completed, shear stress sustained by the sample increases about 4.6% under higher shearing

rate. The rate effect on volumetric strain is more prominent, by the fact that the sample experiences more volume expansion of about 13.5% at the end.

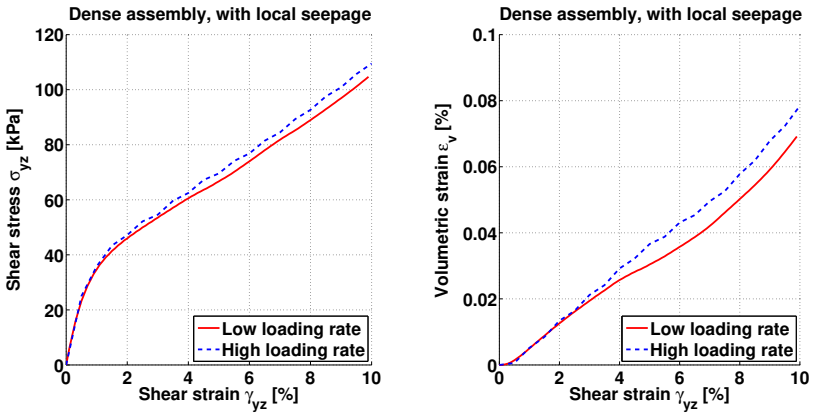

Figure 15: Comparison of global shear stress and global volumetric strain behavior between low loading rate (0.1% shear strain per second) and high loading rate (0.5% shear strain per second), finite strain formulation

4.5 Numerical Example 2: Globally drained triaxial compression test

The third example consists of the globally drained triaxial compression test on an isotropically consolidated cylindrical specimen. This example demonstrates the applicability of the proposed multiscale finite strain scheme on 3D problems. In this numerical example, we analyze (1) the difference between quarter-domain and full-domain simulations for material subjected to axial-symmetrical loading, (2) the consequence of the build-up of excess pore pressure due to a high loading rate and (3) the evolution of the fabric tensor inside and outside the shear band and the implications on the critical state of the materials. As a result, water is allowed to flow through the bottom and the top of the specimen. However, triaxial compression simulation is intentionally not conducted under a fully drained condition at a material point level. Instead, the rate dependence of the constitutive responses introduced via the hydro-mechanical coupling effect is studied to quantify what is the acceptable range of the prescribed loading rate that can prevent significant amount of excess pore pressure.

In addition, microscopic information such as the Biot's coefficient, Biot's modulus and micro-structure fabric are provided to highlight the advantage of the DEM-FEM coupled model. The convergence profile of this simulation is also

presented. In an experimental setting, the drained triaxial test is performed on a cylindrical water-saturated soil specimen, laterally enveloped by rubber membrane and drained through top and bottom surfaces. One of the idealized 3D numerical model constitutes only a quarter of the cylinder by assuming the rotational symmetry. The constant confining pressure is directly applied on the lateral surface, neglecting the effect of rubber membrane. The quasi-static compression is achieved by gradually increasing the axial strain ε_z at the rate of 0.05% per second. The lateral surface is impermeable and a no-flux boundary condition is imposed, while the pore water pressure on both top and bottom surfaces are constrained to be 0. Another simulation is triaxial compression of the full cylindrical domain. Similar confining pressure and pore pressure boundary conditions are applied. The middle point of the bottom surface is fixed to prohibit rigid body translation. The geometry, mesh and boundary conditions of the quarter-/full-domain simulations are illustrated in Fig. 16. The DEM assembly adopted in these simulations is identical to the dense sample in the previous section. The fluid bulk modulus in this example is 2.2 GPa.

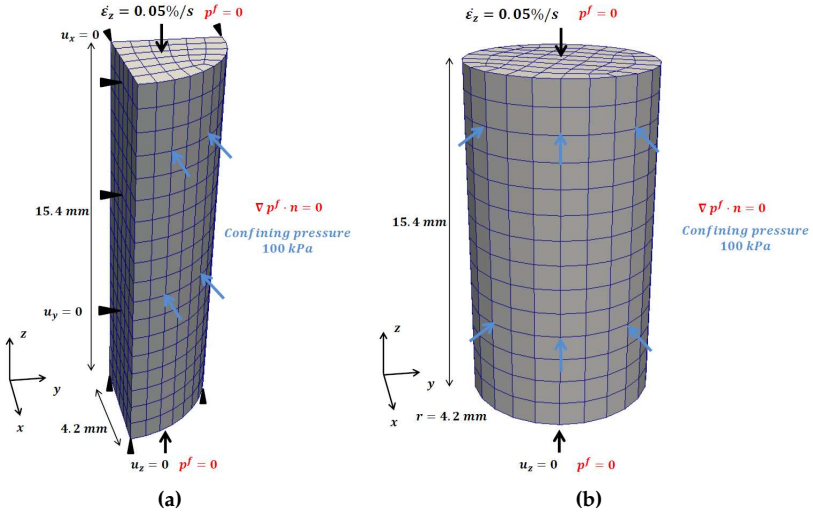

Figure 16: Geometry, mesh and boundary conditions for globally drained triaxial compression test. (a) Quarter-domain simulation. (b) Full-domain simulation

Fig. 17 compares the global shear stress and volumetric strain behavior from quarter-domain and full domain simulations. The shear stress curve obtained from full-domain simulation exhibits less peak stress and more significant softening than quarter-domain simulation. The volumetric strain curves,

however, only show notable difference after the axial strain approaches 7%. This discrepancy may be attributed to the strain localization in full-domain simulation, as shown by the distribution of deviatoric strain and porosity in Fig. 18. A dilatant shear band is developed inside the cylindrical specimen, while in the quarter-domain, the deformation is nearly homogeneous. This difference is more profound given the fact that the proposed model also incorporates the geometrical effect at the finite strain range. Results from this set of simulations show that the quarter-domain simulation is insufficient to capture the deformed configuration when bifurcation occurs. While the assumption of axial-symmetry is valid before the onset of strain localization, enforcing axial-symmetry via reduced domain and additional essential boundary condition may eliminate the bifurcation mode(s) that is not axial-symmetric.

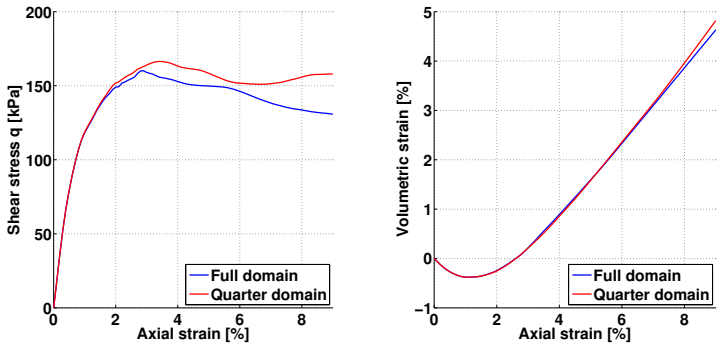

Figure 17: Global shear stress and volumetric strain behavior in globally drained triaxial compression test. Comparison of quarter-domain and full-domain simulations

An additional full-domain simulation is performed at a strain rate ten times slower: $\dot{\epsilon_z} = 0.005\%$ per second. The global shear stress and volumetric strain behavior are compared for the two loading rates in Fig. 19. The specimen under higher strain rate can sustain higher shear stress, but the strain rate has very little influence on volumetric strain behavior. The evolution of pore pressure at the center of the cylindrical specimen in two cases are also shown in Fig. 20. At a high strain rate, the pore water does not have time to fully diffuse through local pores and reach steady state. As a result, excess pore pressure builds up to about 5 kPa while the specimen shrinks. The pressure then decreases and becomes negative when the specimen dilates. In the low-strain-rate case, the magnitude of pore pressure is about five times smaller while the trend looks similar of the high-strain-rate counterpart.

One of the advantages of substituting macroscopic phenomenological consti-

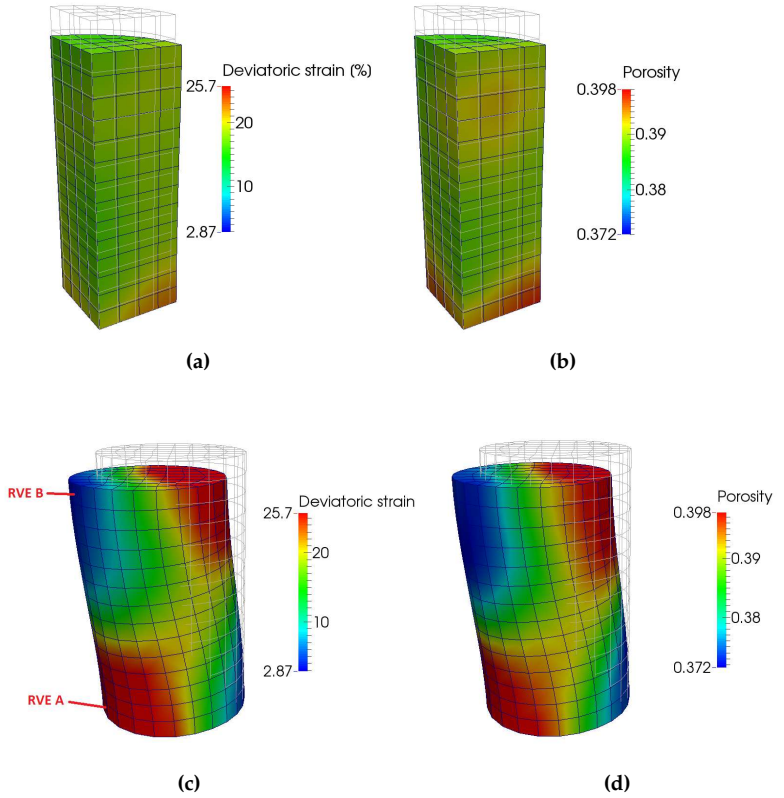

Figure 18: Distribution of deviatoric strain and porosity in globally drained triaxial compression test at 9% axial strain. Comparison of quarter-domain and full-domain simulations.

tutive model with DEM simulations for the poromechanics problem is that the macroscopic poro-elasticity properties, such as Biot's coefficient B, Biot's modulus M and effective permeability k could be inferred and updated from DEM at each Gauss point. As a result, the spatial variability of these poro-elasticity parameters triggered by material bifurcation or non-homogeneous loading can be properly captured. As an example, we monitor the evolution of these poro-elasticity parameters against axial strain ε_z for a RVE inside the shear band (RVE A, shown in Fig. 18(c)) and another RVE outside the shear band (RVE B, shown in Fig. 18(c)) in the $\dot{\epsilon_z} = 0.05\%$-per-second, full-domain simulation (Fig. 21). The evolution of the Biot's coefficient B shown in Fig. 21(a) suggests that the effective bulk modulus of the solid skeleton (K_T^{DEM}) first increases and then decreases presumably due to the porosity changes in both RVEs A and B. The Biot's modulus M, which is related to the Biot's coeffi-

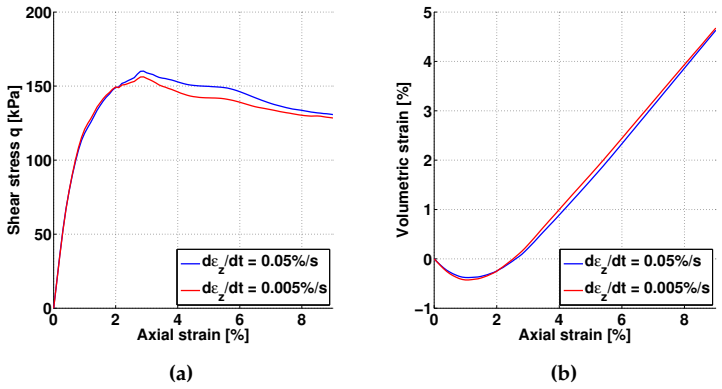

Figure 19: Global shear stress and volumetric strain behavior in globally drained triaxial compression test. Comparison of two loading rate.

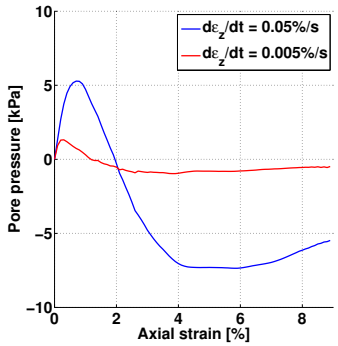

Figure 20: Evolution of pore pressure at the center of the cylindrical specimen during triaxial compression test subjected to two loading rate.

cient B and porosity ϕ, exhibits an initial reduction and largely increases after about $\varepsilon_z = 2\%$ for RVE A. For RVE B, M stays at a constant value. The effective permeability k also evolves with the porosity according to the Kozeny-Carmen relation.

Another advantage of the multiscale scheme is the accessibility to evolution of micro-structures during deformations. To demonstrate this, we perform a simple microstructural analysis in which the Anisotropic Critical State Theory (ACST) introduced by [LD12, ZG13, LD15] is adopted to analyze the fabric of the fluid-saturated granular assemblies at the finite strain range. The fabric anisotropy of two RVEs, one taken inside the shear band (RVE A) and another

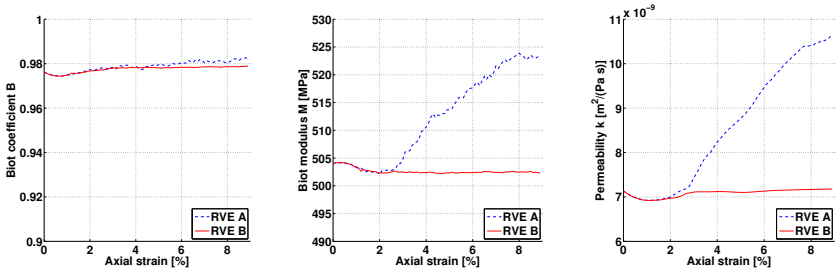

Figure 21: Evolution of (a) Biot's coefficient, (b) Biot's modulus and (c) effective permeability for RVE A (inside shear band, Fig. 18(c)) and RVE B (outside shear band, Fig. 18(c)).

one in the host matrix (RVE B) are analyzed and compared against each other. The fabric tensor $\boldsymbol{G}_{\text{fabric}}$ is contact-normal-based and is computed from a DEM RVE via [LD15]

$$G_{\text{fabric } ij} = \frac{1}{N_c} \sum_{c \in N_c} n_i^c n_j^c \tag{41}$$

where $\boldsymbol{n}^c$ is the unit vector of contact normal and N_c is the number of contacts inside the RVE. The tensor $\boldsymbol{F}_{\text{fabric}}$ characterizes the fabric anisotropy of the RVE and is written as [ZG13]

$$F_{\text{fabric } ij} = \frac{15}{2}(G_{\text{fabric } ij} - \frac{1}{3}\delta_{ij}) \tag{42}$$

where δ_{ij} is the Kronecker delta. Its norm F_{fabric} and direction $\boldsymbol{n}_F$ are defined by

$$\boldsymbol{F}_{\text{fabric}} = F_{\text{fabric}} \boldsymbol{n}_F, \quad F_{\text{fabric}} = \sqrt{\boldsymbol{F}_{\text{fabric}} : \boldsymbol{F}_{\text{fabric}}} \tag{43}$$

To analyze whether and how fabric evolves differently inside shear band and the host matrix, we compute the normalized fabric anisotropy variable (FAV) $A = \boldsymbol{n}_F : \boldsymbol{n}_s$ (a measure introduced in [LD12, ZG13] that quantifies the relative orientation of the tensor $\boldsymbol{F}_{\text{fabric}}$ and the deviatoric stress tensor $\boldsymbol{s}$) for RVE A (inside shear band) and RVE B (outside shear band). The evolution of deviatoric stress q and porosity against axial strain ε_z are also monitored to measure how close the materials in the two RVEs reach the critical state according to the anisotropic critical state theory, i.e.,

$$\eta = \eta_c, \; e = e_c = \hat{e}_c(p) \text{ and } A = A_c = 1 \tag{44}$$

where η is the ratio between the effective mean pressure p' and the deviatoric stress q and e is the void ratio. η_c, $e_c = \hat{e}_c(p)$ and $A_c = 1$ are critical state values of the stress ratio, void ratio and fabric anisotropy variable (cf. [LD12, LD15]).

The results are summarized in Fig. 22. The stress-strain response shown in Fig. 22(a) indicates that RVE A becomes unstable after the peak shear stress and experiences significant dilation until the critical state indicated by the plateau in the porosity curve. The normalized FAV of RVE A rises to about 0.96 quickly upon subjected to the triaxial loading. Then, normalized FAV stay close to 1, which indicates that the fabric and stress directions in RVE A is nearly coaxial, as the RVE A approaches the critical state.

On the other hand, RVE B, which lies outside the shear band, experiences slightly more softening, but the dilatancy is much less than RVE A. The FAV curve of RVE B deviates from the curve of RVE A after axial strain of 2% and exhibits opposite trend that the fabric and stress directions loss coaxiality. This observation suggests that the critical states are not achieved simultaneously within an specimen that forms deformation band.

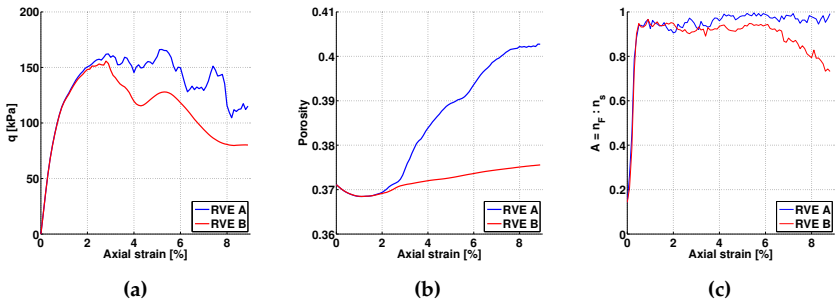

Figure 22: Evolution of (a) deviatoric stress q (b) porosity (c) $A = \boldsymbol{n}_F : \boldsymbol{n}_s$ (relative orientation between anisotropic fabric and deviatoric stress directions) during triaxial compression test ($\dot{\epsilon_z} = 0.05\%/s$) for RVE A (inside shear band, Fig. 18(c)) and RVE B (outside shear band, Fig. 18(c)).

To demonstrate the performance of the multiscale semi-implicit scheme, the convergence rate of the quarter-domain simulation is illustrated in Fig. 23 as an example. At different strain levels, the convergence curves show linear profiles in the logarithm-scale plot. The first step converges the fastest since the RVEs are linear elastic at $\varepsilon_z = 0.1\%$.

The number of iterations required for convergence increases to 11 when the global shear stress reaches the peak (about $\varepsilon_z = 2\%$). In the softening stage, the explicitly treated the elastic-plastic contribution K^{ep} to the material tangential stiffness becomes more significant. Therefore the convergence rate is further reduced and each time step requires about 20 iterations.

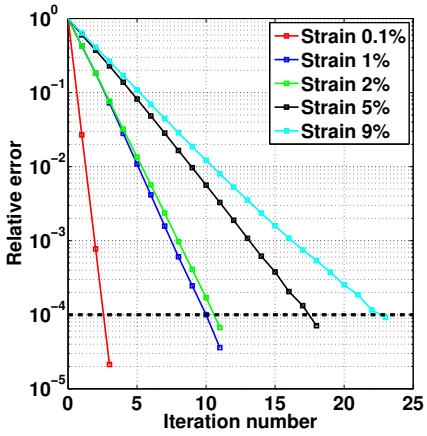

Figure 23: Convergence profiles of the triaxial compression test at different axial strain levels. The relative error is defined as $\frac{||\Delta \boldsymbol{F}^i||}{||\Delta \boldsymbol{F}^{(i=0)}||}$, where $\Delta \boldsymbol{F}^i$ is the residual force at the iteration step i. The convergence is reached when the error falls below 10^{-4}.

5 Multiscale homogenization for embedded discontinuities

Here we present the procedure to obtain the hydro-mechanical constitutive updates for embedded strong discontinuity from microscale simulations on RVEs nested inside the material interfaces. The computational homogenization schemes of single-physics material layers have been explored in a number of previous studies [HRSS09, CKBG12, BKC+14, WS18]. For instance, [HRSS09] have introduced a procedure to generate an effective cohesive zone law for a single interface from microscale RVE. In those studies, FE^2 simulations with interface elements are used as the test bed. [CKBG12, BKC+14] establish a multi-scale approach for RVE (or Microstructural Volume Element as introduced in the literature) having localized zones and proposed a new generalized periodic boundary condition. The overall macro-homogeneous deformation is applied to the MVE and the stress and displacement jump are homogenized. The local equation to be solved is the consistency between the macro displacement jump and the homogenized displacement jump in the RVE, instead of the traction continuity equation. [TSH+14, TSP+16] proposed multiscale model at regular points (MMRp) and singular points (MMSp). It has been successfully used in enhanced strain finite element simulations [OCR+15]. In this study, the RVEs of discrete elements describe the underlying microstructures inside the discontinuity interface. Based on the effective

stress principle, the mechanical and hydraulic constitutive laws are obtained **separately** from two types microscale simulations, i.e. the grain-scale DEM simulation and the pore-scale LBM simulation, as explained in [SKR13] and [WS16]. In other words, the effective traction and the interfacial permeability (and hence the interfacial Darcy's velocity) are both obtained from the same deformed configuration. However, the deformed configuration is not obtained from LBM-DEM simulations but from DEM simulations that generate the admissible boundary conditions by assuming the validity of the effective stress principle. The major advantage of this approach is two-fold. First, the calculations of the interfacial permeability are much faster. This is due to the fact that the de-coupled permeability calculation can be conducted offline such that the trained and validated neural network can be used to replace the costly LB simulations). The second advantage is the simplicity. As the effective stress approach does not require the introduction of particle-scale hydro-mechanical force and any treatment to update the fluid-solid boundary at pore scale. Nevertheless, it should be noted that the validity of this split approach is designed for the case in which the effective stress principle is applicable for the dual-permeability system. In many situations that involve particle erosion [GTSMW15, TPF+17], soil liquefaction [ESA14], or solid-fluid mixture with non-Darcy flow or high Reynold's number, such a simplification may lead to significant errors. In such cases, one must derive the corresponding Hill-Mandel condition for the multi-physical poromechanics problems to obtain the admissible boundary conditions and apply them to the DEM-LBM model or use direct numerical simulation (DNS) to capture the multi-physical problems.

The homogenization procedure of mechanical constitutive law for interface is an extension of the approach described in [HRSS09] to particle assembly using the theory in [MD04, MDZ10]. Consider a domain at the continuum scale discretized by a finite element mesh with enhanced assumed strain or extended finite element to capture the displacement jump kinematics 24.

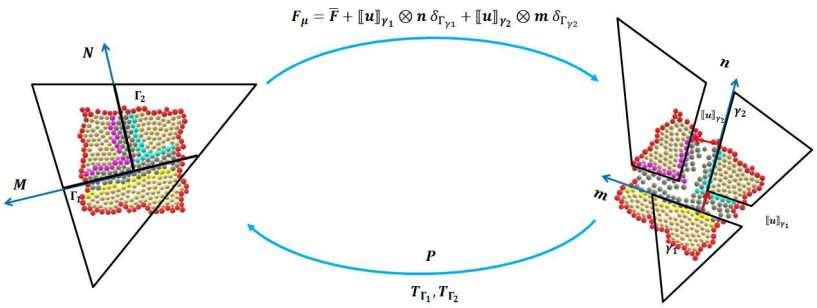

Figure 24: discrete element-informed interface constitutive responses.

At a material point across the interface, there exists a cubic sampled assem-

bly of discrete particles representing the granular material inside the strong discontinuity (Fig. 25). The body force is negligible at micro-scale. This RVE of domain Ω_μ and boundary $\partial\Omega_\mu$ has an initial height of h_μ^0 and is associated with a coordinate system with basis vectors $\boldsymbol{M}_\mu$ and $\boldsymbol{N}_\mu$. Choose the geometric center as the origin and place the RVE in alignment with the normal and tangential directions of the strong discontinuity Γ in the reference configuration ($\boldsymbol{N}_\mu = \boldsymbol{N}$, $\boldsymbol{M}_\mu = \boldsymbol{M}$). The current position $\boldsymbol{x}_\mu^c$ of a center of a particle is related to its position $\boldsymbol{X}_\mu^c$ in the reference configuration via the deformation map $\boldsymbol{\varphi}_\mu$. The local deformation gradient $\boldsymbol{F}_\mu = \frac{\delta \boldsymbol{\varphi}_\mu}{\delta \boldsymbol{X}_\mu^c}$. The volume average of $\boldsymbol{F}_\mu$ is given as:

$$\langle \boldsymbol{F}_\mu \rangle = \frac{1}{V_0} \int_{\Omega_\mu} \boldsymbol{F}_\mu \, d\Omega_\mu = \frac{1}{V_0} \sum_{i}^{N_{bound}} (\boldsymbol{x}_\mu^c)_i \otimes \boldsymbol{A}_i^c, \tag{45}$$

where V_0 is the initial volume of the RVE. $\boldsymbol{A}_i^c$is the surface vector of $\partial\Omega_\mu$ associated with the particle i and N_{bound} is the number of particles on $\partial\Omega_\mu$. Assuming rigid particles, the motion of a particle material point can be decomposed to the motion of the particle center and the particle rotation, i.e.,

$$\boldsymbol{x}_\mu = \boldsymbol{x}_\mu^c + \boldsymbol{R}_\mu \cdot (\boldsymbol{X}_\mu - \boldsymbol{X}_\mu^c); \quad \boldsymbol{x}_\mu^c = \langle \boldsymbol{F}_\mu \rangle \cdot \boldsymbol{X}_\mu^c + \boldsymbol{w}_c, \tag{46}$$

where $\boldsymbol{w}_c$ is the particle center displacement fluctuation and $\boldsymbol{R}_\mu \in SO(3)$ describes the particle rotation.

The overall effective Piola stress is given by the volume average

$$\langle \boldsymbol{P}'_\mu \rangle = \frac{1}{V_0} \int_{\Omega_\mu} \boldsymbol{P}'_\mu \, d\Omega_\mu = \frac{1}{V_0} \sum_{cont}^{Ncont} \boldsymbol{f}_\mu^{cont} \otimes \boldsymbol{L}_\mu^{cont} = \frac{1}{V_0} \sum_{i}^{N_{bound}} (\boldsymbol{f}_\mu^{ext})_i \otimes (\boldsymbol{X}_\mu^c)_i, \tag{47}$$

where $\boldsymbol{f}_\mu^{cont}$ is the contact force at the grain contact $\boldsymbol{x}_\mu^{cont}$. $\boldsymbol{L}_\mu^{cont}$ is the initial branch vector, the vector that connects the centroids of two grains forming the contact. N_{cont} is the total number of particles contacts in the RVE. $(\boldsymbol{f}_\mu^{ext})_i$ is the external support force acting on the boundary particle i. The transition between the summation involving contact forces and the summation involving external support forces is ensured by the equilibrium of the RVE of particles.

The volume average of the virtual power in the RVE is given by

$$\langle \boldsymbol{P}'_\mu : \dot{\boldsymbol{F}}_\mu \rangle = \frac{1}{V_0} \int_{\Omega_\mu} \boldsymbol{P}'_\mu : \dot{\boldsymbol{F}}_\mu \, d\Omega_\mu = \frac{1}{V_0} \sum_{i}^{N_{bound}} (\boldsymbol{f}_\mu^{ext})_i \cdot (\dot{\boldsymbol{x}}_\mu^c)_i. \tag{48}$$

The Hill-Mandel micro-heterogeneity condition requires the volume average of the virtual power in the RVE to equal the virtual power done by the volume averages of power-conjugate stress and deformation measures:

$$\langle \boldsymbol{P}'_\mu : \dot{\boldsymbol{F}}_\mu \rangle = \langle \boldsymbol{P}'_\mu \rangle : \langle \dot{\boldsymbol{F}}_\mu \rangle. \tag{49}$$

Since the constitutive behavior of the RVE is homogenized to a traction-separation law on the interface, the Hill-Mandel condition is recast into the form involving power-conjugate effective traction and displacement jump measures

$$h_0\langle \boldsymbol{P}'_\mu : \dot{\boldsymbol{F}}_\mu \rangle = \langle \boldsymbol{T}'_\Gamma \rangle \cdot \mathscr{L}_v [\![\boldsymbol{u}]\!] = \langle \mathscr{T}_\Gamma \rangle \cdot [\![\dot{\boldsymbol{U}}]\!]. \tag{50}$$

For the transition between the macro-scale kinematics of the strong discontinuity and the deformation of the micro-scale RVE, the volume average of deformation gradient is defined as

$$\langle \boldsymbol{F}_\mu \rangle = \boldsymbol{I} + \frac{1}{h^0_\mu} [\![\boldsymbol{u}]\!] \otimes \boldsymbol{N}. \tag{51}$$

The effective nominal traction $\langle \boldsymbol{T}'_\Gamma \rangle$ averaged in the RVE representing the interface is given by:

$$\langle \boldsymbol{T}'_\Gamma \rangle = \langle \boldsymbol{P}'_\mu \rangle \cdot \boldsymbol{N}. \tag{52}$$

Among the admissible boundary conditions fulfilling the Hill-Mandel micro-heterogeneity condition, we adopt the periodic boundary conditions, where for a pair of particles on opposite boundaries $\partial\mathcal{V}^+$ and $\partial\mathcal{V}^-$, the periodicity enforces the periodicity of fluctuations and rotations

$$\boldsymbol{w}_c^- = \boldsymbol{w}_c^+, \quad \boldsymbol{R}_\mu^- = \boldsymbol{R}_\mu^+, \tag{53}$$

and the anti-periodicity of support forces and couples

$$\boldsymbol{a}_c^- = -\boldsymbol{a}_c^+, \quad \boldsymbol{m}_c^- = -\boldsymbol{m}_c^+, \tag{54}$$

where $\boldsymbol{a}_c$ is the opposite of the resultant force on the boundary particle exerted by other particles, $\boldsymbol{m}_c$ is the opposite of the resultant couple about the center $\boldsymbol{X}_c$ on the boundary particle.

5.1 Offline incremental data-driven hydraulic responses for strong discontinuities

The homogenization procedure used to obtain the effective permeability from a microstructure RVE has been previously studied in [DOS06, OSDKL07, SAR11, SKR13]. Here we apply the same procedure to obtain the homogenized effective permeability of the embedded strong discontinuities. Assume that the separation of the spatial length scale is valid, one may use the Hill-Mandel lemma corresponding to Darcy's flow problem to determine the admissible boundary condition for the flow problems. Recall that the Hill-Mandel lemma requires that

$$\langle \nabla^{\boldsymbol{x}} p_M \cdot \boldsymbol{q}_M \rangle_{\boldsymbol{x}} = \langle \nabla^{\boldsymbol{x}} p_M \rangle_{\boldsymbol{x}} \cdot \langle \boldsymbol{q}_M \rangle_{\boldsymbol{x}} \tag{55}$$

where $\langle\cdot\rangle_{\boldsymbol{x}}$ is the spatial volume averaged operator.

As shown in [DOS06] and [OSDKL07], this can lead to a number of admissible boundary conditions. For instance, one may either prescribe flux or pore pressure gradient in two opposite faces of the RVEs. One interesting aspect found in previous works (cf. [DOS06, SAR11, SKR13, KSW15]) is that the choice of the boundary condition does not affect the effective permeability once the size of the RVE is sufficiently large. We follow the treatment in [dB17] and assume that there is no pore pressure jump across the interface, whereas discontinuous mass flux is admissible.

The effective permeability tensor of a RVE can be determined via inverse fluid flow problem performed on the deformed RVE subjected to prescribed loading paths. The Eulerian fluid flux vector $\boldsymbol{q}$ within the RVE is computed when subjected to Eulerian pressure gradient $\nabla^{\boldsymbol{x}} p$, and the macro-pore effective permeability $\boldsymbol{k}^M_{\mathrm{RVE}}$ is determined by Darcy's law

$$\boldsymbol{q}_M = -\frac{1}{\mu}\boldsymbol{k}^M_{\mathrm{RVE}}\,\nabla^{\boldsymbol{x}}\, p_M. \tag{56}$$

μ is the dynamic viscosity of the fluid. We assume that the normal and tangential directions of the interface are also the principal directions of the macro-pore effective permeability tensors. Thus, we need only two hydraulic simulations to determine the permeability values normal and tangential to the interface, denoted as k^M_n and k^M_m, respectively. Thus the permeability tensor is expressed as

$$\boldsymbol{k}^M_{\mathrm{RVE}} = k^M_n \boldsymbol{n}\otimes\boldsymbol{n} + k^M_m \boldsymbol{m}\otimes\boldsymbol{m}, \tag{57}$$

where $\boldsymbol{n} = \overline{\boldsymbol{F}}\cdot\boldsymbol{N}$ and $\boldsymbol{m} = \overline{\boldsymbol{F}}^{-T}\cdot\boldsymbol{M}$. We choose the lattice Boltzmann (LB) method to solve the inverse fluid flow problem. For brevity, we omit the description of the LB method. Interested readers are referred to [SARE11, SKR13] and [KSW15] for details. The LB code used in this study is a C++ open source code called Palabos [DBBM10]. The procedure to obtain the two normal and tangential components is as follows. We first record the positions of all grains in the deformed microstructural assembly at different strain levels. As the size of each grain is known, the configuration of the pore space can be reconstructed and subsequently converted into binary images (cf. [SKR13]). Then, pore pressure difference is imposed on two opposite sides orthogonal to the flow direction and no-flow boundary conditions are applied on the four remaining side faces. This setting leads to a macroscopic pressure gradient. As the lattice Boltzmann flow simulation reaches steady state, the resultant fluid flow velocity is computed and the permeability value is derived via Darcy's law (Fig. 25). Fig. 28 illustrates an example computation of permeabilities from LBM. The RVE is subjected to various displacement loading paths with loading-unloading cycles. The evolution of normal and tangential permeabilities predicted by the neural network are presented and are compared to the empirical Kozeny-Carman equation.

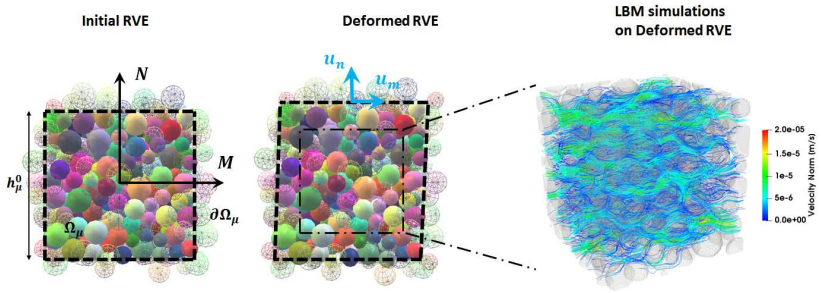

Figure 25: Initial and deformed configurations of the particle assembly representing the granular materials inside strong discontinuity. The effective permeabilities in the normal and tangential directions are determined by Lattice-Boltzmann simulations on representative volume of current particle assembly.

The numerical solutions of Stokes equations using Lattice-Boltzmann method yield accurate results, especially in the low Reynold number regime, but require significant computational resources to resolve the flow field at pore space. To achieve a reasonable accuracy, the number of degree of freedoms required to obtain the effective permeability is at least a few orders more than those used in discrete element simulations [SKR13] Thus, querying the effective permeability tensor from LBM simulations from each RVE for all incremental steps during a multiscale simulation is computationally expensive. In this work, we resort to a deep learning approach to predict the effective permeability for each incremental step. The design, training, and testing of the LSTM network on path-dependent material constitutive laws are detailed in a separate and dedicated work (cf. [WS18]). For completeness, a brief overview is provided.

First, a database containing the prescribed displacement jump loading paths, porosity and associated computed permeabilities is established by running multiple LBM simulations on deformed discrete element RVEs. Then, a recurrent neural network consisting of Long-Short-Term-Memory (LSTM) layers (see Figure 26) is trained using the database generated by LBM simulations [HS97, WS17]. In a nutshell, the training process attempts to minimize an objective function by adjusting the weights of each neuron in the layers through a back-propagation process. The LSTM approach is different than the traditional feed-forward neural network proposed by [GPZHA98] and [LS02] in the sense that (1) the LSTM neuron (see Figure 27) has the capacity to use internal memory to process history and sequence and hence ideal for predictions for path-dependent materials, (2) the LSTM networks are designed to avoid a problem called vanishing or exploding gradient problems that may otherwise lead to issues during the training process.

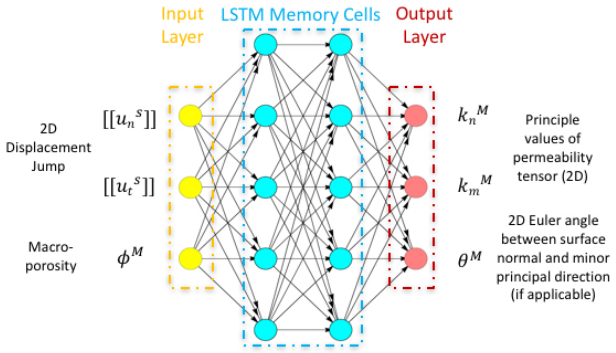

Figure 26: The recurrent neural network used to predict the permeability of the interface.

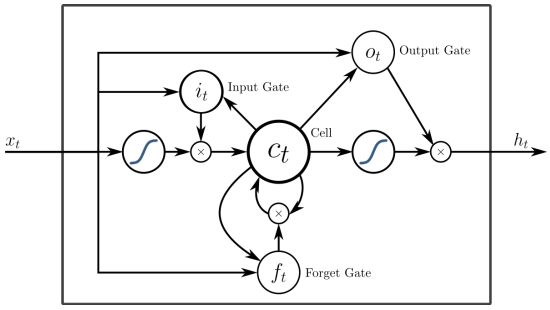

Figure 27: A LSTM block with input, output and forget gates.

Finally, in each incremental update of the multiscale strong discontinuity simulation, the updated effective permeability components are generated by propagating signals from the input layer of the recurrent neural network to the output layers. In this particular case, the current displacement jumps and porosity are used as the input and the principal values and the spectral directions of the effective permeability tensor are the output of the recurrent neural network. One important upshot of this approach is that the querying time is largely reduced, as the deep learning permeability model typically requires only few seconds to make predictions.

5.2 Numerical Example: Reactivation of faults

This example analyzes the slip of a pre-existing and formerly stable fault in saturated soil triggered by the injection of water at a nearby location. The idealized problem geometry and boundary conditions are shown in Fig. 29.

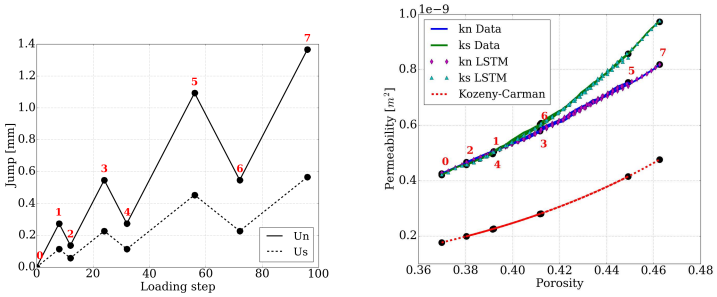

(a) Displacement jump loading path **(b)** Evolution of permeabilities along loading path

Figure 28: Example of permeability data generated from LBM simulations on RVEs undergoing loading-unloading sequences. (a) loading path of the normal Un and tangential displacement jumps Us. (b) Comparison between the normal kn and tangential ks permeability data from LBM simulations and the permeability components from predictions of LSTM neural network model. The calculation from empirical Kozeny-Carman equation $k = \frac{d_{50}^2}{180}\frac{\phi^3}{(1-\phi)^2}$ ($d_{50} = 1mm$) is shown for comparison.

The dimensions of the 2D field of saturated porous media are 10 m x 10 m. The domain is constrained in the x-direction on the left boundary and in the y-direction on the bottom boundary. A foundation has been constructed on top of the domain, generating a uniform loading pressure of 10 MPa. A lateral confining pressure of 5 MPa is applied on the right boundary for the frictional porous media to sustain the vertical load. There exists a 45-degree fault under the foundation. The entire system is stable and has been in equilibrium for a long time since the construction of the foundation, thus the excess pore pressures in both fractures and host matrix are zero. The initial effective stress of the porous solid is hence

$$\sigma'_{\text{Init}} = \begin{bmatrix} -5 & 0 \\ 0 & -10 \end{bmatrix}_{xy} \text{MPa}, \tag{58}$$

where the subscript xy refers to the coordinate system $\{x, y\}$ depicted in Fig. 29.

The DEM RVEs characterizing the traction-separation law of the fault are placed in alignment with the strong discontinuity. They must be in the initial stress state consistent to the macroscopic boundary conditions. From the initial stress state of the macro-scale problem (Eq. 58) and via a coordinate transformation ($\boldsymbol{\sigma}^{mn} = \boldsymbol{R}^{\mathrm{T}} \cdot \boldsymbol{\sigma}^{xy} \cdot \boldsymbol{R}$), the initial stress tensor of the DEM as-

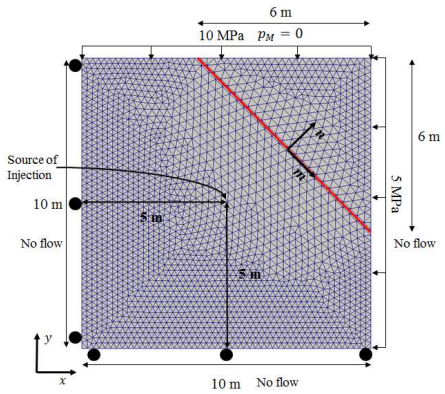

Figure 29: Geometry of fault reactivation problem and boundary conditions. Red line represents the pre-existing fault.

semblies is expressed as

$$\sigma'_{\text{InitRVE}} = \begin{bmatrix} -7.5 & 2.5 \\ 2.5 & -7.5 \end{bmatrix}_{mn} \text{MPa}, \tag{59}$$

where the subscript mn refers to the rotated frame $\{m, n\}$ for the fault depicted in Fig. 29. The initial DEM RVEs in this stress state provide the correct amount of initial shear and normal tractions along the strong discontinuity.

In this example, the particle contact model for DEM is frictional and without cohesion. The normal and tangential permeabilities are obtained from machine learning models trained with LBM simulation data. The bulk material is idealized as isotropic hyperelastic material. The permeability tensors in macro- and micro-pores of the bulk are assumed isotropic and evolve according to the Kozeny-Carman equation. The material parameters used in the numerical example are summarized in [WS19].

Water is injected to the macropore space (pre-existing fractures) of the field through the source S located at the center of the domain. The macropore pressure is zero on the top surface and the other three surfaces are no-flow boundaries. There is no drainage boundary for micropore pressure. This flow boundary condition is to suppress spurious micropore pressure oscillations near the drainage boundary [CB15]. The prescribed time history of Darcy velocity at the source is shown in Fig. 30. The injection profile is composed of injection-pause cycles, in which water supply is provided for 40 hours under a constant rate of 0.02 m/s, followed by a pause for 10 hours before the next cycle of injection. From the simulation results, the time history of the pore pressure in both scales at the source S is presented in Fig. 30. Upon injection or pause, the macropore injection pressure jumps up or plunges immediately,

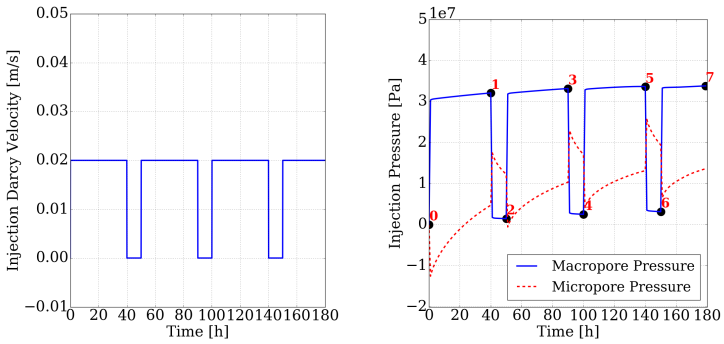

(a) (b)

Figure 30: Water supply in the fault reactivation problem. (a) Time history of the prescribed injection velocity in macropore at the source point. (b) Computed responses of injection pressure in macropore and micropore at the source point. The numbers mark the sequence of injection-pause cycles.

while the micropore pressure at the injection point has the opposite behavior. This is caused by the low mass transfer permeability between the macropores and micropores. Then in the transient regime, when fluid gradually diffuses into the micropores by mass transfer, micropore pressure slowly approaches the macropore pressure. The two pressures will eventually be identical when the diffusion between pores reaches equilibrium.

The macropore and micropore pressure field at time 40 h, 100 h and 180 h are presented in Fig. 31. The pressure plume is initially of the shape of a circle and then expands as the increasing amount of water are being injected through the source. The pore pressure drops when the injection pauses, but the plume is still expanding, driven by the excess pore pressure that has not been entirely diffused. When the injection is resumed, the pore pressure rises again.

The presence of the fault with higher permeability disturbs the pressure plume. The fluid flows more quickly to the top surface through the channel inside the fault. As for the micropore pressure field, it has a similar but delayed evolution behavior, due to the time required for the fluid transfer between macropores and micropores. The difference between macropore and micropore pressure is due to the different permeability in macropores and micropores for the fluid to diffuse in the macro-scale field, and also the low transfer permeability between pores.

Due to the fully coupled nature of the problem, the mechanical responses of the porous solid, especially the displacement jump and traction at the strong discontinuity, strongly depend on how pore fluid diffuses inside the pore

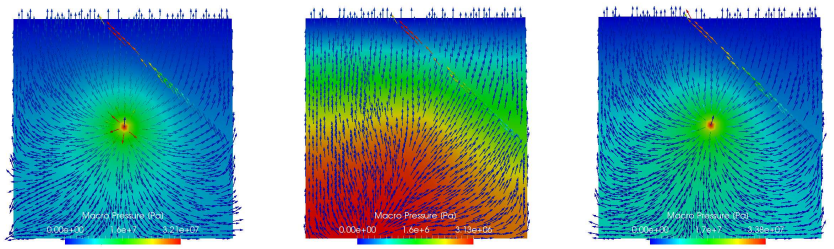

(a) 40 hours **(b)** 100 hours **(c)** 180 hours

(d) 40 hours **(e)** 100 hours **(f)** 180 hours

Figure 31: Evolution of macropore pressure (a-c) and micropore pressure (d-f) field. Arrows indicate the fluid flux vector field in macropores (a-c) and in micropores (d-f). The non-zero components normal to the impervious boundaries are due to the inaccuracy of the nodal projection of the flow vector field evaluated at quadrature points.

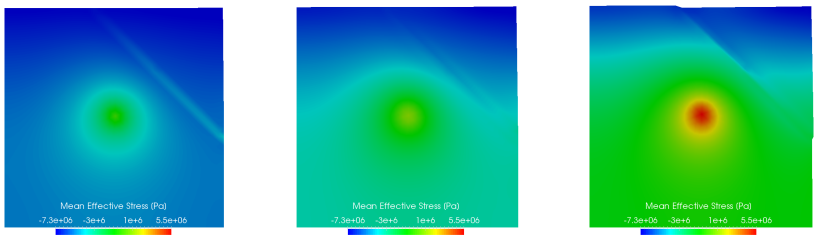

(a) 40 hours **(b)** 100 hours **(c)** 180 hours

Figure 32: Evolution of the mean effective stress field in the macro-scale simulation.

space. The evolution of macro-scale mean effective stress field during the fluid injection cycles is shown in Fig. 32.

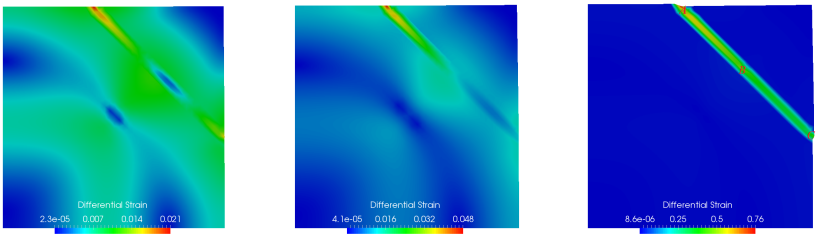

(a) 40 hours **(b)** 100 hours **(c)** 180 hours

Figure 33: Evolution of the differential strain field in the macro-scale simulation.

The increase in the mean effective stress is due to the increase in excess pore pressure, in agreement to the effective stress principle. This results in a reduction in the normal compression traction. As the fault is frictional, this reduction in normal compression also reduce the shear strength and ultimately leads to the reactivation of the fault. The slip can be clearly observed from the changes in deviatoric strain field illustrated in 33. The deviatoric strain gradually increases and concentrates inside the fault zone.

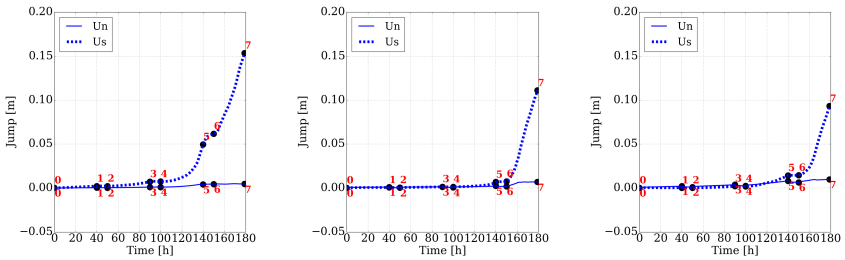

(a) RVE A **(b)** RVE B **(c)** RVE C

Figure 34: History of normal Un and tangential Us components of the displacement jump $[\![\boldsymbol{u}]\!]$ for local RVEs A, B and C (location shown in Fig. 33). The numbers mark the sequence of injection-pause cycles (Fig. 30).

This simulation result suggests the hazardous effect of injecting water to the underground, as a fast fluid flow may trigger the slip of a nearby pre-existing fault, leading to the failure of the foundation.

The Figures clearly illustrate the failure of the fault system by the opening and sliding of the local microstructures, caused by reductions in both normal and

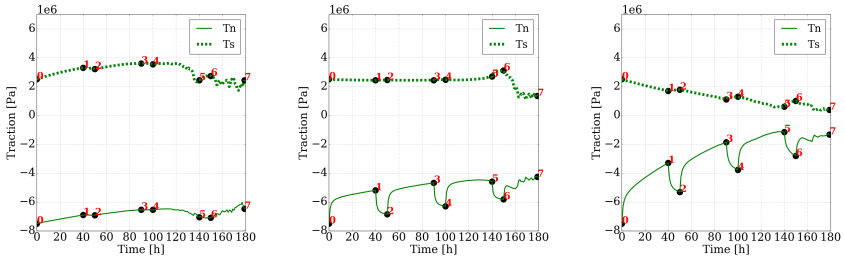

(a) RVE A **(b)** RVE B **(c)** RVE C

The local responses to the fluid injection-pause cycles, including the spatial displacement jump, effective nominal traction and spatial macropore permeability, are illustrated in Fig. 34, Fig. 35 and 36 respectively for three locations A, B, C in the fault indicated in Fig. 33.

Figure 35: History of normal Tn and tangential Ts components of the effective nominal traction $\boldsymbol{T}'$ for local RVEs A, B and C (location shown in Fig. 33). The numbers mark the sequence of injection-pause cycles (Fig. 30).

tangential traction.

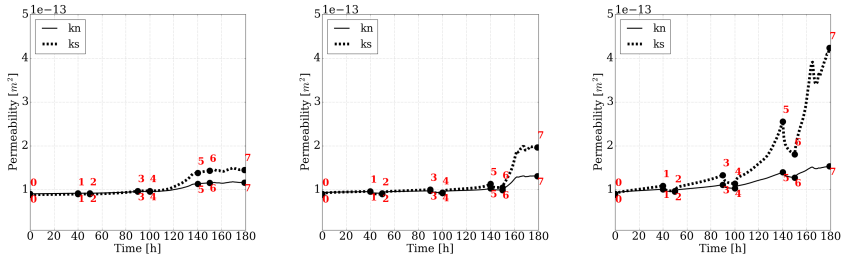

(a) RVE A **(b)** RVE B **(c)** RVE C

Figure 36: History of normal kn and tangential ks components of the macropore permeability $\boldsymbol{k}_{\mathrm{RVE}}$ for local RVEs A, B and C (location shown in Fig. 33). The numbers mark the sequence of injection-pause cycles (Fig. 30).

These results demonstrate the capacity of our proposed multiscale model in capturing the complex mechanical and hydraulic behaviors of the interfacial materials. This is an improvement over the phenomenological traction-separation laws where idealized tensile and shear (linear or exponential) behavior is often adopted [PP11, BS18].

6 Acknowledgements

The author would like to thank his former PhD students, Dr. Kun Wang for contributions on the numerical examples and figures used in this lecture note. The research support by the Earth Materials and Processes program from the US Army Research Office under grant contract W911NF-15-1-0581, the Dynamic Materials and Interactions Program from the Air Force Office of Scientific Research under grant contract FA9550-17-1-0169, the nuclear energy university program from department of energy under grant contract DE-NE0008534, as well as the Mechanics of Materials and Structures program at National Science Foundation under grant contract CMMI-1846875. These supports are gratefully acknowledged. The views and conclusions contained in this document are those of the authors, and should not be interpreted as representing the official policies, either expressed or implied, of the sponsors, including the Army Research Laboratory or the U.S. Government. The U.S. Government is authorized to reproduce and distribute reprints for Government purposes notwithstanding any copyright notation herein.

References

[Arm99] Francisco Armero. Formulation and finite element implementation of a multiplicative model of coupled poro-plasticity at finite strains under fully saturated conditions. *Computer methods in applied mechanics and engineering*, 171(3):205–241, 1999.

[BA95] Ronaldo I Borja and Enrique Alarcón. A mathematical framework for finite strain elastoplastic consolidation part 1: Balance laws, variational formulation, and linearization. *Computer Methods in Applied Mechanics and Engineering*, 122(1):145–171, 1995.

[Bag96] Katalin Bagi. Stress and strain in granular assemblies. *Mechanics of materials*, 22(3):165–177, 1996.

[BBM87] Jacob Bear, Carol Braester, and Pascal C Menier. Effective and relative permeabilities of anisotropie porous media. *Transport in porous media*, 2(3):301–316, 1987.

[BKC+14] Emanuela Bosco, VG Kouznetsova, EWC Coenen, MGD Geers, and Alberto Salvadori. A multiscale framework for localizing microstructures towards the onset of macroscopic discontinuity. *Computational Mechanics*, 54(2):299–319, 2014.

[BS18] Eric C Bryant and WaiChing Sun. A mixed-mode phase field fracture model in anisotropic rocks with consistent kinematics. *Computer Methods in Applied Mechanics and Engineering*, 342:561–584, 2018.

[CB15] Jinhyun Choo and Ronaldo I Borja. Stabilized mixed finite elements for deformable porous media with double porosity. *Computer Methods in Applied Mechanics and Engineering*, 293:131–154, 2015.

[CCB14] Emanuele Catalano, Bruno Chareyre, and Eric Barthélemy. Pore-scale modeling of fluid-particles interaction and emerging poromechanical effects. *International Journal for Numerical and Analytical Methods in Geomechanics*, 38(1):51–71, 2014.

[CKBG12] E WC Coenen, VG Kouznetsova, E Bosco, and M GD Geers. A multi-scale approach to bridge microscale damage and macroscale failure: a nested computational homogenization-localization framework. *International Journal of Fracture*, pages 1–22, 2012.

[CLCC14] Xilin Cui, Jun Li, Andrew Chan, and David Chapman. Coupled dem–lbm simulation of internal fluidisation induced by a leaking pipe. *Powder Technology*, 254:299–306, 2014.

[CMNN81] J Christoffersen, MM Mehrabadi, and S Nemat-Nasser. A micromechanical description of granular material behavior. *Journal of Applied Mechanics*, 48(2):339–344, 1981.

[Cou04] Olivier Coussy. *Poromechanics*. John Wiley & Sons, 2004.

[CS79] Peter A Cundall and Otto DL Strack. A discrete numerical model for granular assemblies. *Geotechnique*, 29(1):47–65, 1979.

[CVW04] Jennifer Sinclair Curtis and Berend Van Wachem. Modeling particle-laden flows: A research outlook. *AIChE journal*, 50(11):2638–2645, 2004.

[dB17] René de Borst. Fluid flow in fractured and fracturing porous media: A unified view. *Mechanics Research Communications*, 80:47–57, 2017.

[DBBM10] Wim Degruyter, Alain Burgisser, Olivier Bachmann, and Orestis Malaspinas. Synchrotron x-ray microtomography and lattice boltzmann simulations of gas flow through volcanic pumices. *Geosphere*, 6(5):470–481, 2010.

[DKU06] Luc Dormieux, Djimédo Kondo, and Franz-Josef Ulm. *Microporomechanics*. John Wiley & Sons, 2006.

[DOS06] X Du and M Ostoja-Starzewski. On the size of representative volume element for darcy law in random media. In *Proceedings of the Royal Society of London A: Mathematical, Physical and Engineering Sciences*, volume 462, pages 2949–2963. The Royal Society, 2006.

[ESA14] Usama El Shamy and Yasser Abdelhamid. Modeling granular soils liquefaction using coupled lattice boltzmann method and discrete element method. *Soil Dynamics and Earthquake Engineering*, 67:119–132, 2014.

[ESZ05] Usama El Shamy and Mourad Zeghal. Coupled continuum-discrete model for saturated granular soils. *Journal of engineering mechanics*, 131(4):413–426, 2005.

[Fis13] Jacob Fish. *Practical multiscaling*. John Wiley & Sons, 2013.

[GAS07] IM Gitman, H Askes, and LJ Sluys. Representative volume: existence and size determination. *Engineering fracture mechanics*, 74(16):2518–2534, 2007.

[GMS13] William G Gray, Cass T Miller, and Bernhard A Schrefler. Averaging theory for description of environmental problems: What have we learned? *Advances in water resources*, 51:123–138, 2013.

[GPZHA98] Jamshid Ghaboussi, David A Pecknold, Mingfu Zhang, and Rami M Haj-Ali. Autoprogressive training of neural network constitutive models. *International Journal for Numerical Methods in Engineering*, 42(1):105–126, 1998.

[GSP09] William G Gray, Bernhard A Schrefler, and Francesco Pesavento. The solid phase stress tensor in porous media mechanics and the hill–mandel condition. *Journal of the Mechanics and Physics of Solids*, 57(3):539–554, 2009.

[GTSMW13] SA Galindo-Torres, A Scheuermann, HB Mühlhaus, and DJ Williams. A micro-mechanical approach for the study of contact erosion. *Acta Geotechnica*, 10(3):357–368, 2013.

[GTSMW15] SA Galindo-Torres, A Scheuermann, HB Mühlhaus, and DJ Williams. A micro-mechanical approach for the study of contact erosion. *Acta Geotechnica*, 10(3):357–368, 2015.

[GZ14] Ning Guo and Jidong Zhao. A coupled fem/dem approach for hierarchical multiscale modelling of granular media. *International journal for numerical methods in engineering*, 99(11):789–818, 2014.

[HC11] Yanhui Han and Peter A Cundall. Lattice boltzmann modeling of pore-scale fluid flow through idealized porous media. *International Journal for Numerical Methods in Fluids*, 67(11):1720–1734, 2011.

[HRSS09] CB Hirschberger, S Ricker, P Steinmann, and N Sukumar. Computational multiscale modelling of heterogeneous material layers. *Engineering Fracture Mechanics*, 76(6):793–812, 2009.

[HS97] Sepp Hochreiter and Jürgen Schmidhuber. Long short-term memory. *Neural computation*, 9(8):1735–1780, 1997.

[JKL03] MJ Jiang, JM Konrad, and S Leroueil. An efficient technique for generating homogeneous specimens for dem studies. *Computers and geotechnics*, 30(7):579–597, 2003.

[KD09] J Kozicki and FV Donzé. Yade-open dem: an open-source software using a discrete element method to simulate granular material. *Engineering Computations*, 26(7):786–805, 2009.

[KRMK14] Matthew R Kuhn, Hannah E Renken, Austin D Mixsell, and Steven L Kramer. Investigation of cyclic liquefaction with discrete element simulations. *Journal of Geotechnical and Geoenvironmental Engineering*, 140(12):04014075, 2014.

[KSW15] Matthew R Kuhn, WaiChing Sun, and Qi Wang. Stress-induced anisotropy in granular materials: fabric, stiffness, and permeability. *Acta Geotechnica*, 10(4):399–419, 2015.

[LD12] Xiang Song Li and Yannis F Dafalias. Anisotropic critical state theory: role of fabric. *Journal of Engineering Mechanics*, 138(3):263–275, 2012.

[LD15] XS Li and YF Dafalias. Dissipation consistent fabric tensor definition from dem to continuum for granular media. *Journal of the Mechanics and Physics of Solids*, 78:141–153, 2015.

[LMW12] Anders Logg, Kent-Andre Mardal, and Garth Wells. *Automated solution of differential equations by the finite element method: The FEniCS book*, volume 84. Springer Science & Business Media, 2012.

[LS02] M Lefik and BA Schrefler. Artificial neural network for parameter identifications for an elasto-plastic model of superconducting cable under cyclic loading. *Computers & structures*, 80(22):1699–1713, 2002.

[MD04] Christian Miehe and Joachim Dettmar. A framework for micro–macro transitions in periodic particle aggregates of granular materials. *Computer Methods in Applied Mechanics and Engineering*, 193(3):225–256, 2004.

[MDZ10] C Miehe, J Dettmar, and D Zäh. Homogenization and two-scale simulations of granular materials for different microstructural constraints. *International Journal for Numerical Methods in Engineering*, 83(8-9):1206–1236, 2010.

[MNBT13] Mario J Martinez, Pania Newell, Joseph E Bishop, and DZ Turner. Coupled multiphase flow and geomechanics model

for analysis of joint reactivation during co 2 sequestration operations. *International Journal of Greenhouse Gas Control*, 17:148–160, 2013.

[NB71] Amos Nur and JD Byerlee. An exact effective stress law for elastic deformation of rock with fluids. *Journal of Geophysical Research*, 76(26):6414–6419, 1971.

[NCDD11] Michał Nitka, Gaël Combe, Cristian Dascalu, and Jacques Desrues. Two-scale modeling of granular materials: a dem-fem approach. *Granular Matter*, 13(3):277–281, 2011.

[Ng06] Tang-Tat Ng. Input parameters of discrete element methods. *Journal of Engineering Mechanics*, 132(7):723–729, 2006.

[OCR+15] J Oliver, M Caicedo, Emmanuel Roubin, Alfredo Edmundo Huespe, and JA Hernández. Continuum approach to computational multiscale modeling of propagating fracture. *Computer Methods in Applied Mechanics and Engineering*, 294:384–427, 2015.

[OSDKL07] Martin Ostoja-Starzewski, X Du, ZF Khisaeva, and W Li. Comparisons of the size of the representative volume element in elastic, plastic, thermoelastic, and permeable random microstructures. *International Journal for Multiscale Computational Engineering*, 5(2), 2007.

[PP11] Kyoungsoo Park and Glaucio H Paulino. Cohesive zone models: a critical review of traction-separation relationships across fracture surfaces. *Applied Mechanics Reviews*, 64(6):060802, 2011.

[Pre82] J. H. Prevost. Nonlinear transient phenomena in saturated porous media. *Computer Methods in Applied Mechanics and Engineering*, 30(1):3 – 18, 1982.

[RRL14] Martin Robinson, Marco Ramaioli, and Stefan Luding. Fluid–particle flow simulations using two-way-coupled mesoscale sph–dem and validation. *International journal of multiphase flow*, 59:121–134, 2014.

[SAR11] WaiChing Sun, José E. Andrade, and John W. Rudnicki. Multiscale method for characterization of porous microstructures and their impact on macroscopic effective permeability. *International Journal for Numerical Methods in Engineering*, 88(12):1260–1279, 2011.

[SARE11] WaiChing Sun, José E Andrade, John W Rudnicki, and Peter Eichhubl. Connecting microstructural attributes and permeability from 3d tomographic images of in situ shear-enhanced compaction bands using multiscale computations. *Geophysical Research Letters*, 38(10), 2011.

[ŠCC+10] V Šmilauer, E Catalano, B Chareyre, S Dorofeenko, J Duriez, A Gladky, J Kozicki, C Modenese, L Scholtès, L Sibille, et al. Yade documentation. *The Yade Project.(http://yade-dem. org/doc/)*, 2010.

[SKR13] WaiChing Sun, Matthew R. Kuhn, and John W. Rudnicki. A multiscale dem-lbm analysis on permeability evolutions inside a dilatant shear band. *Acta Geotechnica*, pages 1–16, 2013.

[SOS13] WaiChing Sun, Jakob T. Ostien, and Andrew G. Salinger. A stabilized assumed deformation gradient finite element formulation for strongly coupled poromechanical simulations at finite strain. *International Journal for Numerical and Analytical Methods in Geomechanics*, 37(16):2755–2788, 2013.

[SSD95] RB Saeger, LE Scriven, and HT Davis. Transport processes in periodic porous media. *Journal of Fluid Mechanics*, 299:1–15, 1995.

[Suc01] Sauro Succi. *The lattice Boltzmann equation: for fluid dynamics and beyond*. Oxford university press, 2001.

[SWZP86] B.R. Simon, J.S.-S. Wu, O.C. Zienkiewicz, and D.K. Paul. Evaluation of u – w and u – π finite element methods for the dynamic response of saturated porous media using one-dimensional models. *International Journal for Numerical and Analytical Methods in Geomechanics*, 10(5):461–482, 1986.

[TPF+17] DK Tran, N Prime, F Froiio, Carlo Callari, and E Vincens. Numerical modelling of backward front propagation in piping erosion by dem-lbm coupling. *European Journal of Environmental and Civil Engineering*, 21(7-8):960–987, 2017.

[TSH+14] Sebastian Toro, Pablo J Sánchez, Alfredo Edmundo Huespe, Sebastian Miguel Giusti, Pedro J Blanco, and RA Feijóo. A two-scale failure model for heterogeneous materials: numerical implementation based on the finite element method. *International Journal for Numerical Methods in Engineering*, 97(5):313–351, 2014.

[TSP+16] Sebastian Toro, PJ Sánchez, JM Podestá, PJ Blanco, Alfredo Edmundo Huespe, and RA Feijóo. Cohesive surface model for fracture based on a two-scale formulation: computational implementation aspects. *Computational mechanics*, 58(4):549–585, 2016.

[TTE+43] Karl Terzaghi, Karl Terzaghi, Civil Engineer, Austria Czechoslowakia, Karl Terzaghi, Ingénieur Civil, Autriche Tchécoslovaquie, and Etats Unis. *Theoretical soil mechanics*, volume 18. Wiley New York, 1943.

[WBF06] Joshua A White, Ronaldo I Borja, and Joanne T Fredrich. Calculating the effective permeability of sandstone with multiscale

lattice boltzmann/finite element simulations. *Acta Geotechnica*, 1(4):195–209, 2006.

[WLW08] C Wellmann, C Lillie, and P Wriggers. Homogenization of granular material modeled by a three-dimensional discrete element method. *Computers and Geotechnics*, 35(3):394–405, 2008.

[Woo90] David Muir Wood. *Soil behaviour and critical state soil mechanics*. Cambridge university press, 1990.

[WS16] Kun Wang and WaiChing Sun. A semi-implicit discrete-continuum coupling method for porous media based on the effective stress principle at finite strain. *Computer Methods in Applied Mechanics and Engineering*, 304:546 – 583, 2016.

[WS17] Kun Wang and WaiChing Sun. Data-driven discrete-continuum method for partially saturated micro-polar porous media. In *Poromechanics VI*, pages 571–578. 2017.

[WS18] Kun Wang and WaiChing Sun. A multiscale multi-permeability poroplasticity model linked by recursive homogenizations and deep learning. *Computer Methods in Applied Mechanics and Engineering*, 334:337–380, 2018.

[WS19] Kun Wang and WaiChing Sun. An updated lagrangian lbm–dem–fem coupling model for dual-permeability fissured porous media with embedded discontinuities. *Computer Methods in Applied Mechanics and Engineering*, 344:276–305, 2019.

[YIV98] Mitsutoshi Yoshimine, Kenji Ishihara, and William Vargas. Effects of principal stress direction on intermediate principal stress on undrained shear behavior of sand. *Soils and Founcations*, 38(3):179–188, 1998.

[ZG13] Jidong Zhao and Ning Guo. Unique critical state characteristics in granular media considering fabric anisotropy. *Géotechnique*, 63(8):695–704, 2013.

[ZH82] AA Zick and GM Homsy. Stokes flow through periodic arrays of spheres. *Journal of fluid mechanics*, 115:13–26, 1982.

[ZH97] Qisu Zou and Xiaoyi He. On pressure and velocity boundary conditions for the lattice boltzmann bgk model. *Physics of fluids*, 9(6):1591–1598, 1997.

[ZW01] TI Zohdi and P Wriggers. Computational micro-macro material testing. *Archives of Computational Methods in Engineering*, 8(2):131–228, 2001.

Laboratoire 3SR / Bâtiment Galilée
CS 40700
38 058 Grenoble cedex 9
France

ISBN 978-2-9561359-6-8

Fon: +33 (0) 456 528 621
Fax: +33 (0) 476 827 043
president@alertgeomaterials.eu
http://alertgeomaterials.eu